



LUND UNIVERSITY

The Bunch-by-Bunch Feedback System in the MAX IV 3 GeV Ring

Olsson, David; Malmgren, Lars; Karlsson, Anders

2017

Document Version:

Publisher's PDF, also known as Version of record

[Link to publication](#)

Citation for published version (APA):

Olsson, D., Malmgren, L., & Karlsson, A. (2017). *The Bunch-by-Bunch Feedback System in the MAX IV 3 GeV Ring*. (Technical Report LUTEDX/(TEAT-7253)/1-48/(2017); Vol. 7253). MAX-lab, Lund University.

Total number of authors:

3

General rights

Unless other specific re-use rights are stated the following general rights apply:

Copyright and moral rights for the publications made accessible in the public portal are retained by the authors and/or other copyright owners and it is a condition of accessing publications that users recognise and abide by the legal requirements associated with these rights.

- Users may download and print one copy of any publication from the public portal for the purpose of private study or research.
- You may not further distribute the material or use it for any profit-making activity or commercial gain
- You may freely distribute the URL identifying the publication in the public portal

Read more about Creative commons licenses: <https://creativecommons.org/licenses/>

Take down policy

If you believe that this document breaches copyright please contact us providing details, and we will remove access to the work immediately and investigate your claim.

LUND UNIVERSITY

PO Box 117
221 00 Lund
+46 46-222 00 00

The Bunch-by-Bunch Feedback System in the MAX IV 3 GeV Ring

David Olsson, Lars Malmgren, and Anders Karlsson

Electromagnetic Theory
Department of Electrical and Information Technology
Lund University
Sweden



David Olsson
david.olsson@maxiv.lu.se

MAX IV Laboratory
Lund University
P.O. Box 118
SE-221 00 Lund
Sweden

Lars Malmgren
lars.malmgren@maxiv.lu.se

MAX IV Laboratory
Lund University
P.O. Box 118
SE-221 00 Lund
Sweden

Anders Karlsson
anders.karlsson@eit.lth.se

Department of Electrical and Information Technology
Electromagnetic Theory
Lund University
P.O. Box 118
SE-221 00 Lund
Sweden

This is an author produced preprint version as part of a technical report series from the Electromagnetic Theory group at Lund University, Sweden. Homepage <http://www.eit.lth.se/teat>

Abstract

The MAX IV facility in Lund, Sweden consists of two storage rings for production of synchrotron radiation. The larger 3 GeV ring has been delivering light to the first users since November 2016, while the smaller 1.5 GeV ring is being commissioned. Coupled-Bunch Mode Instabilities (CBMIs) have been observed in both rings, and they have a degrading effect on the beam quality since they increase the effective emittance and the energy spread. In order to suppress CBMIs, a digital Bunch-By-Bunch (BBB) feedback system has been commissioned in the 3 GeV ring. The feedback in the three planes has this far been two provided by two striplines kickers. A waveguide overloaded cavity kicker, dedicated for feedback in the longitudinal plane, will soon be commissioned. Apart from applying negative feedback, the BBB feedback system is a comprehensive diagnostic tool. The design of the feedback kickers and the implementation of the BBB feedback system in the 3 GeV ring are presented in this report. Initial results from instability studies are also discussed.

Contents

1	Introduction	2
2	Coupled-bunch Mode Instabilities	3
2.1	Beam Dynamics in a Storage Ring	3
2.2	Drivers of CBMIs	5
2.2.1	Vacuum Chamber Discontinuities	6
2.2.2	Resistive Wall Instabilities	6
2.2.3	Ion-induced Instabilities	6
2.3	Methods to Suppress CBMIs	6
2.3.1	Negative Feedback	7
2.3.2	Harmonic Cavities	7
2.3.3	Damping of HOMs	8
2.3.4	Shifting Cavity HOMs in Frequency	9
2.3.5	Non-uniform Filling Patterns	10
2.3.6	Phase Modulation	10
3	Design of Striplines	11
3.1	Geometry	11
3.2	Electromagnetic Properties	11
3.3	Measurements	16
4	Design of a Waveguide Overloaded Cavity	17
4.1	Geometry	17
4.2	Cavity Requirements	19
4.3	Cavity Body	20
4.4	Cavity Matching	22
4.5	Wakefields and Heat Load	25

4.6	Vacuum Port	28
4.7	Measurements	28
5	The BBB Feedback System	31
5.1	BBB Feedback in the 3 GeV Ring	32
5.1.1	Front-End	32
5.1.2	Signal Processing Units	34
5.1.3	Back-End	35
5.1.4	Complete Set-up	38
5.2	BBB Feedback in the 1.5 GeV Ring	38
6	Beam Measurements	40
6.1	Diagnostic Measurements	40
6.2	Bunch Cleaning	41
6.3	Feedback Effect on Beam Quality	42
6.3.1	Transverse Feedback	42
6.3.2	Longitudinal Feedback	43
7	Conclusions and Future Work	46
A	Stripline S-parameter Measurements	49

1 Introduction

The MAX IV facility in Lund, Sweden consists of two storage rings, where the larger 3 GeV ring is designed for production of high-brilliance hard X-ray synchrotron light, and the smaller 1.5 GeV ring will produce light in the IR to the soft X-ray spectral range [26]. The 3 GeV has currently five beamlines in operation, and this ring has delivered light to the first users since November 2016, while the first beamlines in the 1.5 GeV ring will be commissioned in the autumn of 2017.

In order to provide high-brightness synchrotron light to the users, the electron beam has to be stable in all three planes. Since the electron bunches couple to each other via wakefields, they can under certain resonance conditions drive coherent coupled-bunch oscillations. Such oscillations are called Coupled-Bunch Mode Instabilities (CBMIs). They can increase the effective emittance and the energy spread of the beam which thereby decreases the brilliance at the beamlines. In order to suppress these CBMIs, both rings will operate with Bunch-By-Bunch (BBB) feedback systems. The commissioning of the BBB feedback system in the 3 GeV ring started in early 2016, while the commissioning in the 1.5 GeV ring will start in the autumn of 2017. The focus of this report is therefore on the 3 GeV BBB feedback system and on the beam measurements performed there.

A brief introduction to CBMIs and their effect on the electron beam is given in Section 2. The driving sources of the CBMIs and different ways to suppress them are also discussed in that section. The feedback signal is applied via kickers (actuators), and striplines have this far been used as actuators in all three planes.

The stripline design is presented in Section 3. Section 4 describes the design of a waveguide overloaded cavity that will soon be the dedicated actuators in the longitudinal plane (the two striplines will still provide feedback in the horizontal and in the vertical plane). The basic principles and the layout of the BBB feedback system in the 3 GeV ring is described in Section 5. Finally, some measurements on how the BBB feedback system affects the beam properties are presented in Section 6. In this section, it is shown how the quality of the light seen at the beamlines is affected by CBMIs and that they can be suppressed by the BBB feedback system.

2 Coupled-bunch Mode Instabilities

The main purpose of the BBB feedback system is to damp CBMIs since they have a degrading effect on the quality of the synchrotron light seen at the beamlines. CBMIs and the collective effects that are driving them is a vast and complex topic, and only a brief introduction to the physics necessary to understand the basic concept of CBMIs and BBB feedback systems is therefore presented in this section. A more comprehensive and very intuitive guide on bunch-by-bunch feedback systems can be found in the Cern Accelerator School material provided by M. Lonza [17]. For more in-depth information on CBMIs and other collective effects, [19] is recommended.

2.1 Beam Dynamics in a Storage Ring

In circular accelerators, the displacement of a particle from its ideal orbit is described by the equation of motion

$$x''(t) + 2Dx'(t) + \omega^2x(t) = 0 \quad (2.1)$$

where $D = \tau_D^{-1}$ is the radiation damping, and τ_D is the radiation damping time. Since the particle emits synchrotron radiation, $D > 0$ and then the excited oscillations are damped. $x(t)$ can describe the displacement in any of the three planes. When (2.1) describes the horizontal/vertical motion, then ω is the horizontal/vertical betatron angular frequency, and when it describes the motion in the longitudinal plane, then ω is the synchrotron angular frequency. If we assume that $\omega \gg D$, the solution to (2.1) is approximated by an exponentially damped sinusoidal oscillation

$$x(t) = Ae^{-Dt} \cos(\omega t + \phi) \quad (2.2)$$

where A and ϕ are an arbitrary amplitude and phase, respectively. In reality, the displacement of a single electron is not entirely damped until it propagates along its ideal orbit since it experiences smaller excitations continuously due to quantum excitations when emitting light. Quantum excitations of the electrons is the main contributor to the finite energy spread (also known as the natural energy spread) of the beam, and appears because synchrotron radiation is emitted in discrete packets of photons. Excitations do also occur due to collisions between the electrons. This is known as intrabeam scattering, and becomes more notable at higher beam currents.

The size of a stable beam is therefore not zero, and its average size in phase space is given by its emittance.

In, (2.1), all oscillations are damped, and the electrons in a single bunch are oscillating around their ideal orbit incoherently. However, there is an electromagnetic coupling between the bunches via wakefields. Under certain resonance conditions, the wakefields might drive the electrons in a single bunch so that they oscillate coherently around their ideal orbit. These oscillations are known as coupled-bunch oscillations. That modifies the equation of motion to

$$x''(t) + 2(D - G)x'(t) + \omega^2 x(t) = 0 \quad (2.3)$$

with the solution

$$x(t) = Ae^{-(D-G)t} \cos(\omega t + \phi) \quad (2.4)$$

where G is the growth rate driven by the wakefields, and $\tau_G = G^{-1}$ is the growth time. If $G > D$, the beam becomes unstable, and the oscillations grow exponentially, which leads to an excited CBMI. If the oscillations grow larger than what is allowed by the acceptance of the storage ring, then the exponential growth can result in beam loss. For smaller values of G , the CBMI might not result in beam loss since non-linear effects saturate the amplitude of the oscillations before they grow so large that the beam is lost. If this is the case, the effects of transverse CBMIs can be seen as an increased transverse beam size and thereby as an increase of the effective emittance. Longitudinal CBMIs result in an increased energy spread which also increases the beam size due to dispersion. It will be shown in Section 6.3 that CBMIs have a degrading effect on the quality of the beam and the brightness of the light seen at the beamlines. Since G is proportional to the beam current, it is always possible to keep the beam stable below the current threshold where the CBMI is excited.

The number of Coupled-Bunch Modes (CBMs) that can be excited depends on the filling pattern in the storage ring. If all the ring buckets are filled, the number of possible CBMIs is the same as the number of bunches, i.e., the same as the harmonic number of the accelerator. As mentioned above, the electrons oscillate coherently at their betatron/synchrotron frequency when a CBMI is excited. The index of the CBM that is excited determines how the centroids of the bunches oscillate relative to each other, i.e., the phase advance $\Delta\phi$ of the oscillations between each bunch. If all the M buckets in the storage ring are filled (as in normal operation at MAX IV), $\Delta\phi$ is given by

$$\Delta\phi = m \frac{2\pi}{M} \quad (2.5)$$

where $m = 0, 1, \dots, M - 1$ is the index of the CBM. Each excited CBM appears in the beam spectrum as an infinite number at resonance peaks at

$$f = pf_{\text{RF}} \pm (m + \nu)f_0 \quad (2.6)$$

where $f_{\text{RF}} = Mf_0$ is the frequency of the RF system, f_0 is the revolution frequency, ν is the fractional betatron/synchrotron tune, and $p \in \mathbb{Z}$. One important observation

from (2.6) is that it is sufficient to monitor a frequency span of $f_{\text{RF}}/2$ centred around $f = f_{\text{RF}}(1/4 + n/2)$, $n \in \mathbb{N}$ in order to observe an excited CBMI. To illustrate this, assume that we have a storage ring with $M = 8$ equally spaced bunches, the circumference L , and a vertical fractional tune of $\nu = 0.33$. Then, Figure 1 (a) shows the vertical displacement of the 8 bunches at a given time when the vertical CBM #1 ($m = 1$) and CBM #5 ($m = 5$) are excited compared to a stable beam. Figure 1 (b) shows the corresponding beam spectrum in the span $0 \leq f \leq f_{\text{RF}}$ for the three cases.

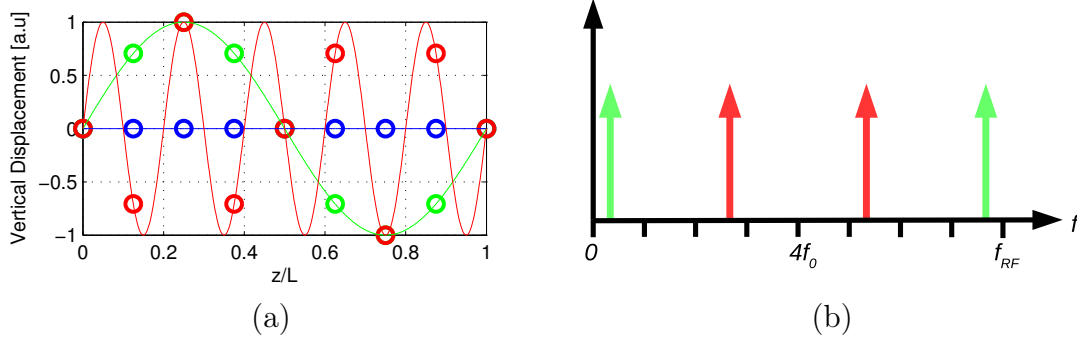


Figure 1: (a) shows the maximum vertical displacement of the 8 bunches at a given time for a stable beam (blue circles), when CBM #1 ($m = 1$, green circles) is excited, and when CBM #5 ($m = 5$, red circles) is excited. Here, $M = 8$, $\nu = 0.33$, z is the longitudinal position, and L is the circumference of the storage ring. (b) shows the corresponding vertical beam spectrum lines for CBM #1 (green) and CBM #5 (red).

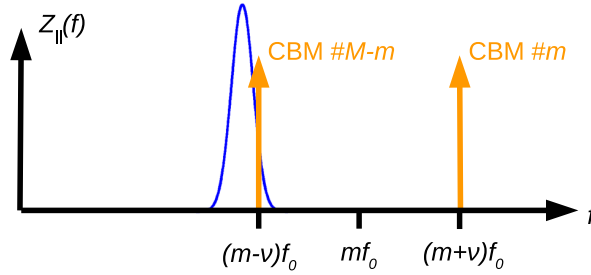


Figure 2: The longitudinal beam impedance, $Z_{||}(f)$, around a cavity HOM (blue line). The two orange lines are the spectrum lines of CBM number m and $M - m$ ($p = 0$). As seen, the spectrum line of the latter overlaps with the impedance response of the HOM, and that CBM can therefore be excited.

2.2 Drivers of CBMIs

As mentioned in the previous section, CBMIs are driven by wakefields. Below we list the sources of the wakefields that give a coupling between bunches.

2.2.1 Vacuum Chamber Discontinuities

Wakefields from a single bunch can be reflected at discontinuities in the vacuum chambers and affect the motion of succeeding bunches. This can be the driving source of both transverse and longitudinal CBMIs. Examples of such discontinuities are tapers, BPM buttons, bellows, RF fingers, pumping ports, and accelerator cavities.

In the longitudinal plane, the instabilities are often driven by high-Q eigenmodes trapped in the vacuum chambers since the stored energy in these eigenmodes can grow quite large due to coherent multi-turn wakefield superposition. At MAX IV, many of the Higher-Order Modes (HOMs) in the main and in the Landau cavities are such high-Q eigenmodes. These HOMs can drive CBMIs if their beam impedance spectrum overlaps with the frequencies of the CBMs in (2.6), as illustrated in Figure 2. Since these eigenmodes are very narrowbanded, it is sometimes possible to shift them in frequency and thereby avoid excitations of CBMIs as described in Section 2.3.4.

2.2.2 Resistive Wall Instabilities

The beam induces mirror currents on the inside of the vacuum chambers as it propagates in the accelerator. Since the beam chambers are made of materials with a finite conductivity, the mirror currents experience resistive losses. These losses assert a decelerating force on the bunches which is proportional to the beam current. The decelerating forces can drive CBMIs, and they are especially strong in low-gap chambers (such as in-vacuum undulators/wigglers). One of the reasons for using copper (a high-conductivity material) chambers in the 3 GeV ring is to reduce the risks of resistive wall instabilities. Resistive wall instabilities can appear both in the longitudinal and in the transverse plane, but is often a problem in the latter.

2.2.3 Ion-induced Instabilities

Ions in the vacuum chambers can drive ion-electron coherent oscillations that result in transverse CBMIs. The ions, which are created when the beam is colliding with gas molecules in the non-perfect vacuum, are trapped in the negative potential of the beam and they are accumulated over several beam passages. Normally, the beam current threshold, where the ion-induced instabilities appear, increases with time as the vacuum improves. This was also observed at MAX IV which is reported in Section 6.3.1.

2.3 Methods to Suppress CBMIs

In the early design phase of an accelerator, one should reduce the risks of CBMIs. By carefully designing the vacuum chambers, one can make sure that the geometrical wake impedance is minimized. It is then important to reduce the impact of high-Q eigenmodes that are trapped in the structures. As already mentioned, materials with low resistivity in the walls of the vacuum chambers reduce the impact of resistive-wall

instabilities, and a good quality of the vacuum suppresses ion-induced instabilities. However, once the accelerator is running and the "damage has been done", there are several ways to suppress the CBMIs that hopefully makes it possible to operate the storage ring with a stable beam at the nominal beam current. Some methods that are used or considered at MAX IV are listed below.

2.3.1 Negative Feedback

The most straightforward way to suppress a CBMI is to damp the coherent oscillations with negative feedback. A BBB feedback system is here applying a kick to each single bunch for every revolution. The kick signal is sinusoidal and proportional to the derivative of the coherent oscillation so that the equation of motion from Section 2.1 becomes

$$x''(t) + 2(D + D_{fb} - G)x'(t) + \omega^2 x(t) = 0 \quad (2.7)$$

where D_{fb} is the damping term from the feedback. We see that stability is achieved if $(D + D_{fb} - G) > 0$. As mentioned in Section 2.1, it is sufficient to monitor a carefully chosen span of $f_{RF}/2$ in order to observe all the CBMs in the beam spectrum. The same goes for the feedback signal, i.e., the feedback kickers should have a bandwidth (BW) of at least $f_{RF}/2$ in order to suppress all the CBMIs. The BBB feedback system in MAX IV is presented in detail in Section 5.

2.3.2 Harmonic Cavities

Both MAX IV storage rings are equipped with passive 3:rd harmonic (Landau) cavities that provide bunch lengthening up to a factor five compared to a single 100 MHz RF system [2]. The bunch lengthening decouples the high-frequency part of the impedance spectrum of the machine from the beam, i.e., the impedance spectrum at higher frequencies has little effect on the beam since the spectrum of each bunch becomes more narrow as the bunch length increases. For example, the loss factor $\kappa_{||}$ in (4.9) is reduced as $\lambda(\omega)$ becomes more narrow. A very important consequence of the bunch lengthening is that it reduces the excitation of the cavity HOMs that are driving longitudinal CBMIs, and thereby increases the current threshold where the beam becomes unstable.

The Landau cavities also increase the spread of the synchrotron frequency (tune spread) among the electrons in a single bunch. The tune spread increases with the non-linearity of the RF waveform [19]. With a single RF system, the RF waveform is sinusoidal and is quite linear at the synchronous phase unless the total maximum voltage provided by the RF system per turn is close to the voltage lost by the electrons as synchrotron radiation per turn. When the Landau cavities are excited for optimum bunch lengthening, the superposed RF waveform forms a plateau (the derivative is zero) at the synchronous phase and is therefore more non-linear. The tune spread has a damping effect on CBMIs since it reduces the coherency of the driven bunch oscillations. This is also known as Landau damping.

Simulation model	f_c [MHz]	Q
No HOM damper	101.91	21502
	407.18	34786
	460.38	36920
One HOM damper	101.90	21370
	406.99	1299
	459.38	746

Table 1: The resonance frequencies f_c and quality factors Q of the first three main cavity eigenmodes, with and without HOM dampers. The simulations are done in COMSOL [9].

Apart from reducing the impacts of collective effects, the bunch lengthening also decreases the electron density which increases the Touschek lifetime and reduces the transverse emittance.

2.3.3 Damping of HOMs

In the early design phase of MAX IV, there were plans to attach at least one HOM damper to each main cavity. The purpose of the dampers is to increase the external loading of the unwanted HOMs and thereby to decrease their quality factors as described in [16]. By doing so, the growth rates of the CBMs driven by the HOMs are reduced.

An in-air HOM damper prototype for the MAX IV main cavities has been developed. The prototype consists of a coaxial structure that forms a notch filter (rejection filter) around 100 MHz (around the cavity fundamental mode). The coaxial structure is inserted into the cavity lateral surface, and it couples to the cavity magnetic fields via a loop antenna. The other end of the structure is terminated with a $50\ \Omega$ load. Figure 3 (a) shows a simulation model of the HOM damper inserted into a main cavity, and (b) shows the prototype inserted into a vented cavity. By tuning the notch filter to the frequency of the fundamental mode, many of the HOMs can be damped, while the coupling to the fundamental mode is negligible. Table 1 shows the resonance frequency and quality factors of the fundamental and the first two HOMs in a main cavity, with and without the prototype HOM damper. As seen, the fundamental mode is quite unaffected by the HOM damper, while the two HOMs are heavily damped. Note that the input coupling loop for the 100 MHz RF power is not included in the model. The plan to implement HOM dampers is currently on hold, and it will be evaluated if the combination of Landau cavities and a BBB feedback system is sufficient to suppress all the longitudinal CBMs up to the design current of 500 mA.

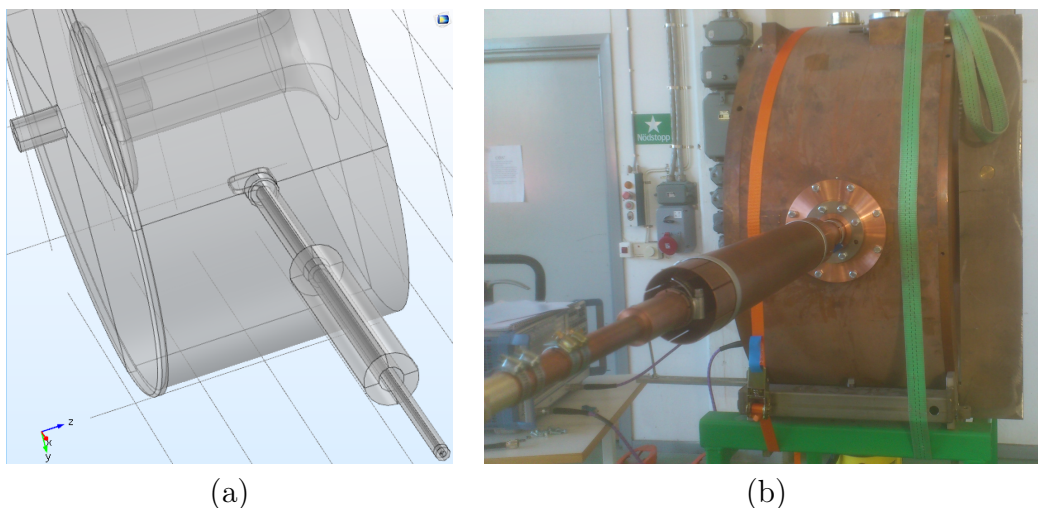


Figure 3: (a) shows the HOM damper prototype together with a MAX IV main cavity in COMSOL, and (b) shows the prototype when it is inserted into a vented cavity.

2.3.4 Shifting Cavity HOMs in Frequency

Another passive way to decrease the impact of CBMs is to shift the frequencies of the cavity HOMs and move them away from the spectrum lines of any harmful CBMs (see Figure 2). There are two ways to shift the frequencies of the cavity eigenmodes. The first method is to move the position of the cavity end plates with a mechanical tuning system. The second method is to change the temperature of the cavity with the cooling water, and thereby change the cavity volume due to the expansion/contraction of the copper. When tuning the cavities, the aim is to keep the frequency of the fundamental modes constant, and shift frequencies of the HOMs. Thus for every new cavity temperature (within the operational span), there exists an end plate position where the frequency of the fundamental mode is unchanged. Since the HOMs are responding differently to mechanical and temperature tuning compared to the fundamental mode, the new combination of end plate position and temperature will shift the HOMs in frequency. An extensive study on how the eigenmodes in the main and Landau cavities respond to mechanical and temperature tuning can be found in [6].

This method is being used together with negative feedback in the longitudinal plane in order to continuously increase the beam current threshold where the beam becomes unstable. With the BBB feedback system it is possible to perform grow/damp transient measurements (see Section 6.1) just below the current threshold where the stability is lost and to see which CBM that has the highest growth rate. That particular CBM is then the reason why stability is lost at a slightly higher current. The next step is to identify which cavity the HOM that is driving the CBM is originating from by tuning the end plates and the temperature of the cavities. When the problematic cavity is found (for some reason, it is always the last

cavity you investigate...), the HOMs of that cavity are shifted in frequency, and it is now hopefully possible to keep the beam stable at higher currents. The procedure is then repeated just below the new threshold where the beam goes unstable. These studies are often very time consuming.

2.3.5 Non-uniform Filling Patterns

There are some advantages of operating a storage ring with non-uniform filling patterns. For example, if ion-induced CBMIs are a problem, one can introduce a gap in the filling pattern. By doing so, the negative potential of the beam is distorted, and it might prevent trapping of ions if the gap is large enough. Such gap is also known as an ion-clearing gap. The effects on the beam performance after introducing an ion-clearing gap is reported in [25].

Since the bunches couple to each other via wakefields, it is also possible to increase the longitudinal tune spread by introducing gaps in the filling pattern. Note that we are here mainly increasing the tune spread among the bunches, and not among electrons in each bunch as in the case with harmonic cavities. This technique has been used at MAX IV at lower currents in order to keep the beam stable.

Non-uniform filling patterns can be achieved in MAX IV by selecting the ring buckets that are injected by adjusting the chopper [3] or by doing bunch cleaning with the BBB feedback system (see Section 6.2).

2.3.6 Phase Modulation

One active method to suppress longitudinal CBMIs that is being used with success at LNLS is to phase modulate the RF fields in the main cavities [1]. With the phase modulation activated, the signal delivered to a main cavity, $V_{\text{RF}}(t)$, becomes

$$V_{\text{RF}}(t) = \hat{V} \cos(\omega_{\text{RF}}t + \hat{\phi}_{\text{mod}} \cos(\omega_{\text{mod}}t + \varphi_{\text{mod}}) + \varphi_{\text{RF}}) \quad (2.8)$$

where \hat{V} and $\hat{\phi}_{\text{mod}}$ are the amplitude of the RF voltage and the phase modulation respectively. φ_{RF} and φ_{mod} are arbitrary phases, and ω_{RF} and ω_{mod} are the frequencies of the main RF system and the phase modulation, respectively. At LNLS, ω_{mod} is set to a value close to twice that of the synchrotron frequency, and the effect of phase modulation is that the electrons in each bunch are split up into two (or three) bunchlets, each with slightly different synchrotron frequencies. The phase modulation increases the Landau damping by an increase of the longitudinal tune spread in the bunches.

This far, LNLS has been operating with a single-RF system (no bunch lengthening with harmonic cavities), and this is when phase modulation is most advantageous. However, one drawback with phase modulating the main RF signal is that it increases the energy spread within the bunches. At MAX IV, phase modulation is therefore a tool that might be useful at lower beam currents to keep the beam stable where there are no significant Landau damping due to bunch lengthening. At date, it is not possible to phase modulate the main RF signal, but the required modifications to the LLRF system would be rather small [21].

3 Design of Striplines

As mentioned, stripline kickers are used as actuators when applying transverse feedback. Two striplines for the BBB feedback system are installed in the 3 GeV ring, one for excitation in each plane. Striplines offer several advantages such as, high transverse shunt impedance, simple design, short rise and fall times, and they can be operated directly in the baseband (BB) span of 0-50 MHz, which is where the signal processing units operate (see Section 5.1.2). The striplines can also simultaneously be used as weak actuators for feedback in the longitudinal plane. This is possible by upconverting the BB signal to a frequency range where the striplines have higher longitudinal shunt impedance (see Section 5.1.3).

Since the in-vacuum parts of the two striplines are identical (they are only rotated 90 degrees relative to each other during installation), only the horizontal stripline is analysed. The electromagnetic properties of a stripline are covered in detail in [20], and no detailed analysis is therefore given in this report.

3.1 Geometry

The design of the striplines for the BBB feedback system is a modified version of the design in [20]. Except for the dimensions, the two major differences are that the new striplines only have two strips each, and that they have tapering sections at the ends of the strips.

The main chamber, the strips, and the flanges are made of stainless steel 316. Figure 4 (a) shows a 3D model of the chamber. Figure 4 (b) shows a 2D cross section of the stripline mid section, where $a = 13.5$ mm, $a_g = 25.2$ mm, $\phi_s = 107.20$ degrees, and $\phi_g = 12.75$ degrees. The length of each strip (feedthrough-to-feedthrough) is $L = 300$ mm, and the total length of the vacuum chamber (flange-to-flange) is 400 mm. Each strip has two tapered sections that make the transition between the feedthroughs and the stripline mid section in Figure 4 (b) less abrupt. The length of each tapered section is $L_t = 25$ mm, and they are visible in Figure 4 (a). Besides from improving the transmission line impedance matching, the tapers also reduce the beam impedance of the stripline at higher frequencies, as shown in Section 3.2. Figure 5 shows one of the manufactured striplines.

3.2 Electromagnetic Properties

The electric scalar potential, $\Phi(\rho, \phi)$, can be obtained analytically by solving Laplace equation over a transverse cross section of the geometry, which is shown in [20]. $\Phi(\rho, \phi)$ is here limited to the region where $0 \leq \rho \leq a$ and requires that the stripline is evaluated far away from its end-gaps. $\mathbf{E}(\rho, \phi)$ and $\mathbf{H}(\rho, \phi)$ are then obtained as $-\nabla\Phi(\rho, \phi)$ and $\frac{j}{\mu_0\omega}\nabla \times \mathbf{E}(\rho, \phi)$, respectively.

The first propagating TEM modes are the odd (differential) and even (common) modes. The potentials of the two strips have the same magnitudes but different polarities in odd mode ($U_1 = V_0$ and $U_2 = -V_0$ in Figure 4 (b)), and the scalar

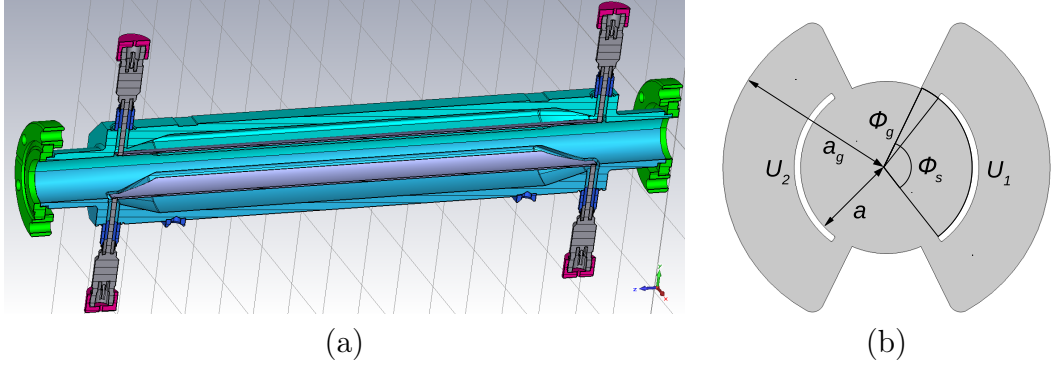


Figure 4: (a) shows a 3D cross section of the stripline, and (b) shows a 2D cross section with some of its dimensions.



Figure 5: The manufactured vacuum chamber of the vertical stripline.

potential $\Phi_{\perp}(\rho, \phi)$ for this mode can be expanded in a Fourier series

$$\Phi_{\perp}(\rho, \phi) = \frac{8V_0}{\pi\phi_g} \sum_{n=1,3,5,\dots}^{\infty} \left(\frac{\rho}{a}\right)^n \frac{\sin\left(n\frac{\phi_g}{2}\right) \sin\left(n\frac{\phi_s+\phi_g}{2}\right)}{n^2} \cos(n\phi) \quad (3.1)$$

In the even mode, the two strips both have the same potential ($U_1 = U_2 = V_0$), and the Fourier series $\Phi_{\parallel}(\rho, \phi)$ becomes

$$\Phi_{\parallel}(\rho, \phi) = V_0 \frac{\phi_g + \phi_s}{\pi} + \frac{8V_0}{\pi\phi_g} \sum_{n=2,4,6,\dots}^{\infty} \left(\frac{\rho}{a}\right)^n \frac{\sin\left(n\frac{\phi_g}{2}\right) \sin\left(n\frac{\phi_s+\phi_g}{2}\right)}{n^2} \cos(n\phi) \quad (3.2)$$

Figure 6 shows $\Phi(\rho, \phi)$ obtained in (3.1) and (3.2) (upper figure), together with electrostatic simulations of the same modes in COMSOL (lower figure). The longitudinal and transverse geometry factors, g_{\parallel} and g_{\perp} , defined in [14] are

$$g_{\parallel} = \frac{\Phi_{\parallel}(\rho=0)}{V_0} = \frac{\phi_s + \phi_g}{\pi} = 0.67 \quad (3.3)$$

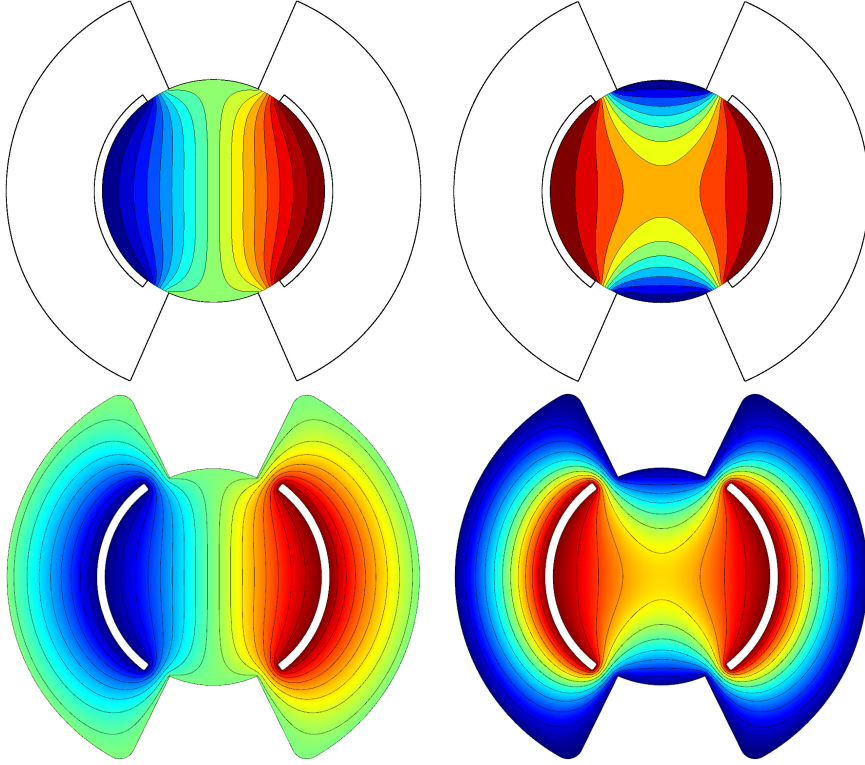


Figure 6: $\Phi(\rho, \phi)$ obtained analytically in (3.1) and (3.2) (upper), and numerically in COMSOL (lower). The left figures show the odd mode, and the right ones show the even mode.

$$g_{\perp} = \frac{a|E_x(\rho=0)|}{V_0} = \frac{8}{\phi_g \pi} \sin\left(\frac{\phi_g}{2}\right) \sin\left(\frac{\phi_s + \phi_g}{2}\right) = 1.10 \quad (3.4)$$

A design goal is to make the deflecting field as homogeneous as possible in the vicinity of the beam. Figure 7 shows $E_x(x, y=0)/E_x(\rho=0)$ and $E_x(x=0, y)/E_x(\rho=0)$ for different values of ϕ_s . As seen, a quite good homogeneity is obtained when $\phi_s = 107.2$ degrees.

Since the characteristic impedance of the surrounding RF system is $Z_0 = 50 \, \Omega$, each strip should be matched to this impedance in order to avoid reflections when the strips are excited by the amplifiers and/or by the beam itself. The strips are loaded differently in the odd and even mode which results in different impedances. An optimization approach that can be found in the literature is $Z_0 \approx \sqrt{Z_{0,\perp} Z_{0,\parallel}}$, where $Z_{0,\perp}$ and $Z_{0,\parallel}$ are the characteristic impedance of a single strip in the odd and even mode, respectively. The gap at the outer side of the strips are therefore adjusted to fulfil this relationship. With the stripline dimensions mentioned above, $Z_{0,\perp} = 47.2 \, \Omega$ and $Z_{0,\parallel} = 52.9 \, \Omega$.

As mentioned, the transmission line impedance matching is improved by implementing the two tapered sections to each strip. The geometry of the tapers and the grounded regions close to the them are optimized for the best possible S-parameters, both when the stripline is fed in common and in differential-mode. There are also

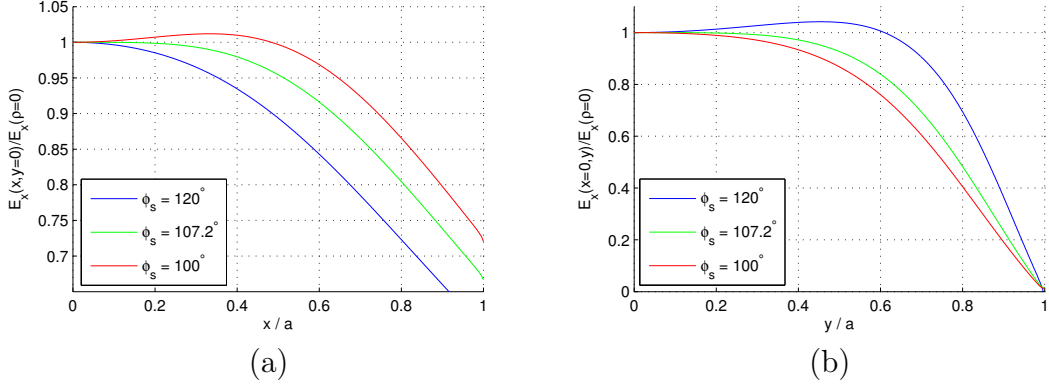


Figure 7: $E_x(x, y = 0)/E_x(\rho = 0)$ (a) and $E_x(x = 0, y)/E_x(\rho = 0)$ (b) obtained as $-\nabla\Phi(\rho, \phi)$ from (3.1) for different ϕ_s . Here, ϕ_g and a are set to 12.75 degrees and 13.5 mm, respectively.

some production limits that must be considered such as the minimum radius of the tools and the milling angle. In Section 3.3, the simulated S-parameters are compared with the measured S-parameters for one of the manufactured striplines.

The low-frequency approximation of the longitudinal and transverse (horizontal) beam impedance, $Z_{||}(\omega)$ and $Z_x(\omega)$, are give by (3.5) and (3.6), respectively. As seen, the last term makes the beam impedance converge to zero at higher frequencies due to the tapers [4]. Figure 8 shows $Z_{||}(\omega)$ and $Z_x(\omega)$ obtained in GdfidL [13] up to 10 GHz. Note that the ceramic feedthroughs are simplified as simple coaxial lines in these simulations. The loss factor, $\kappa_{||}$, and the dissipated power, P_{loss} , due to the beam impedance are listed in Table 2. Almost all of the beam induced power is dissipating in the coaxial high-power loads that are connected to the upstream stripline ports.

$$Z_{||}(\omega) = \frac{Z_{0,||}g_{||}^2}{4} \left(2 \sin^2 \left(\frac{\omega(L - L_t)}{c_0} \right) + j \sin \left(\frac{2\omega(L - L_t)}{c_0} \right) \right) \frac{\sin^2 \left(\frac{\omega L_t}{c_0} \right)}{\left(\frac{\omega L_t}{c_0} \right)^2} \quad (3.5)$$

$$Z_x(\omega) = \frac{c_0 Z_{0,\perp}}{2} \left(\frac{g_{\perp}}{a} \right)^2 \frac{1}{\omega} \left(2 \sin^2 \left(\frac{\omega(L - L_t)}{c_0} \right) + j \sin \left(\frac{2\omega(L - L_t)}{c_0} \right) \right) \frac{\sin^2 \left(\frac{\omega L_t}{c_0} \right)}{\left(\frac{\omega L_t}{c_0} \right)^2} \quad (3.6)$$

An approximation of the transverse and longitudinal shunt impedances, $R_{\perp}(\omega)$ and $R_{||}(\omega)$, are given by (3.7) and (3.8). In these two equations, it is assumed that the stripline is fed in differential and common-mode, respectively. Figure 9 shows $R_{\perp}(\omega)$ and $R_{||}(\omega)$ obtained analytically and from frequency domain simulations in COMSOL. In the simulations, the ceramic and dielectric losses in the chamber are

included, and all the sub components of the coaxial feedthroughs are included as well.

$$R_{\perp}(\omega) = 2Z_{0,\perp} \left(\frac{g_{\perp} c_0}{a} \right)^2 \frac{\sin^2 \left(\frac{\omega(L-L_t)}{c_0} \right)}{\omega^2} \frac{\sin^2 \left(\frac{\omega L_t}{c_0} \right)}{\left(\frac{\omega L_t}{c_0} \right)^2} \quad (3.7)$$

$$R_{\parallel}(\omega) = 4 \operatorname{Re}(Z_{\parallel}(\omega)) = 2Z_{0,\parallel} g_{\parallel}^2 \sin^2 \left(\frac{\omega(L-L_t)}{c_0} \right) \frac{\sin^2 \left(\frac{\omega L_t}{c_0} \right)}{\left(\frac{\omega L_t}{c_0} \right)^2} \quad (3.8)$$

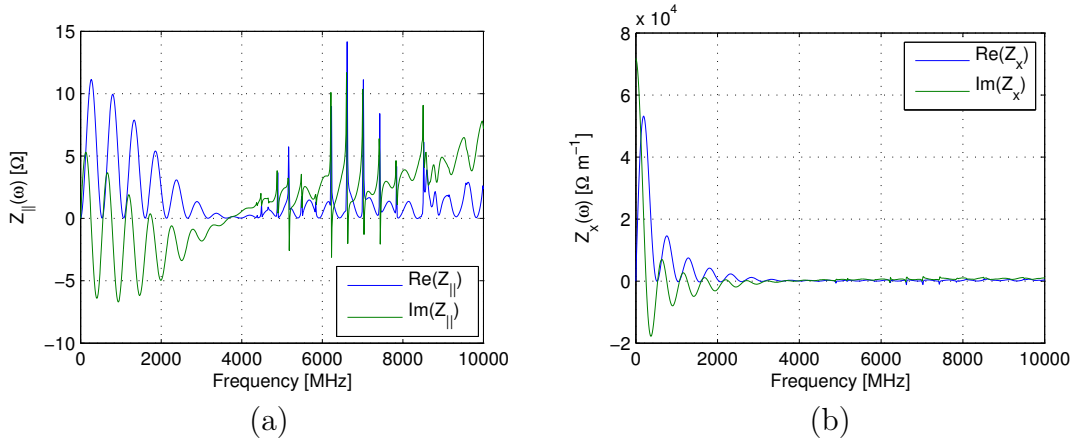


Figure 8: $Z_{\parallel}(\omega)$ (a) and $Z_x(\omega)$ (b) of the stripline obtained in GdfidL.

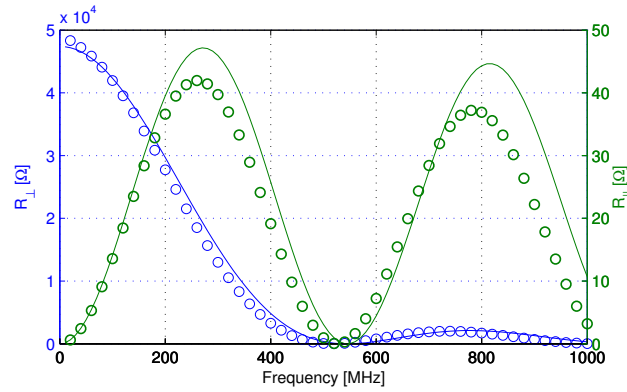


Figure 9: $R_{\perp}(\omega)$ and $R_{\parallel}(\omega)$ obtained from (3.7)-(3.8) (solid lines) and from COM-SOL (circles).

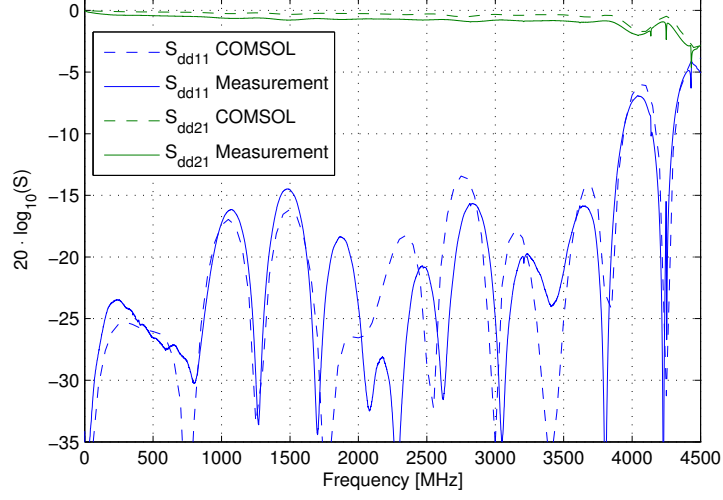


Figure 10: S_{dd11} and S_{dd21} of a stripline obtained from COMSOL and from a measurement.

Guassian $\sigma = 40$ mm		Quartic $\sigma = 56$ mm	
$\kappa_{ }$ [mV/pC]	P_{loss} [W]	$\kappa_{ }$ [mV/pC]	P_{loss} [W]
10.5	26.3	7.70	19.3

Table 2: The loss factor, $\kappa_{||}$, and the dissipated power, P_{loss} , in a stripline due to the beam impedance for two different bunch profiles. P_{loss} is obtained for a uniform filling pattern at a total beam current of 500 mA.

3.3 Measurements

The simulated differential and common-mode S-parameters are shown in Figure 10 and 11, respectively. The simulations are performed with the frequency domain solver in COMSOL with all the details and material parameters of the coaxial feedthroughs included. Dielectric losses in the ceramic and the resistive losses in the metal walls are also included in the simulations. The differential-mode parameters, S_{dd11} and S_{dd21} , are the reflection and transmission parameters, respectively when applying transverse feedback in BB, i.e., feeding the two strips with opposite polarities. Similar, the common-mode parameters, S_{cc11} and S_{cc21} correspond to the S-parameters when applying longitudinal feedback via the stripline back-end, as described in 5.1.3. The same S-parameters obtained from measurements of the vertical stripline are also shown in the figures. Here, a 4-port VNA is used, and the set-up during the mixed-mode measurements is the same as described in [20]. As seen, there is a quite good agreement to the simulations, even though the simulations slightly underestimate the transmission losses (up to 0.25 dB in the stripline operational range). The complete result from the mixed-mode measurements of both striplines are shown in Figure 50-57 in Appendix A.

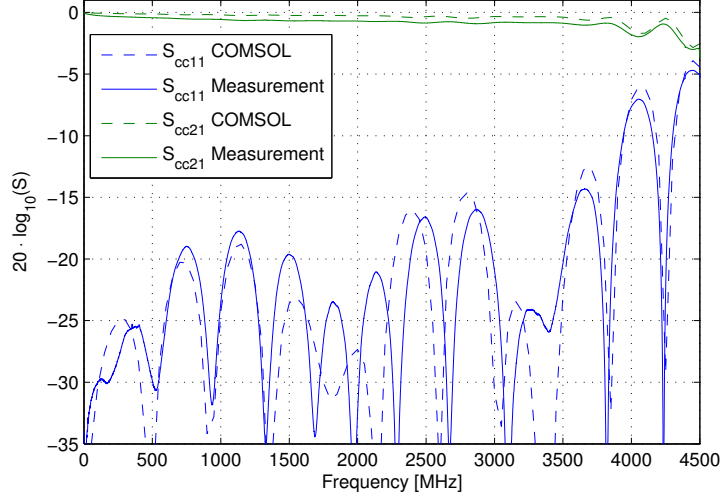


Figure 11: S_{cc11} and S_{cc21} of a stripline obtained from COMSOL and from a measurement.

There are some visible narrow-banded notches above 4 GHz in the measured data in Figure 10. These notches are trapped eigenmodes, similar to those described in [20]. The eigenmodes are not studied further since they are considered too weak and located too high up in frequency in order to have any notable effect on the beam quality.

4 Design of a Waveguide Overloaded Cavity

As explained in Section 3, the two striplines were initially used both as longitudinal and transverse actuators. A waveguide (WG) overloaded cavity was designed as a designated longitudinal actuator, and it was installed in the 3 GeV ring in July 2017. Overloaded cavities are used as longitudinal actuators at several facilities, and most of them are based on the DAΦNE design which was developed in the mid 90's [7]. The main advantage of an overloaded cavity compared to a stripline is its much higher longitudinal shunt impedance in the former.

4.1 Geometry

The basic components of the cavity are a standard stainless steel pipe and two copper bodies. Figure 12 shows a 3D model of the assembled cavity. The steel pipe has an inner radius of 100 mm, and four smaller pipes with CF16 flanges are attached to its lateral surface. Coaxial N-type feedthroughs are attached to the CF16 flanges. The steel pipe also has one attached pipe with a CF75 flange for an ion pump. Cavity nose cones and four ridged WGs are milled into the copper bodies. Each copper body is braced to a steel flange and then attached to the flanges that are welded to

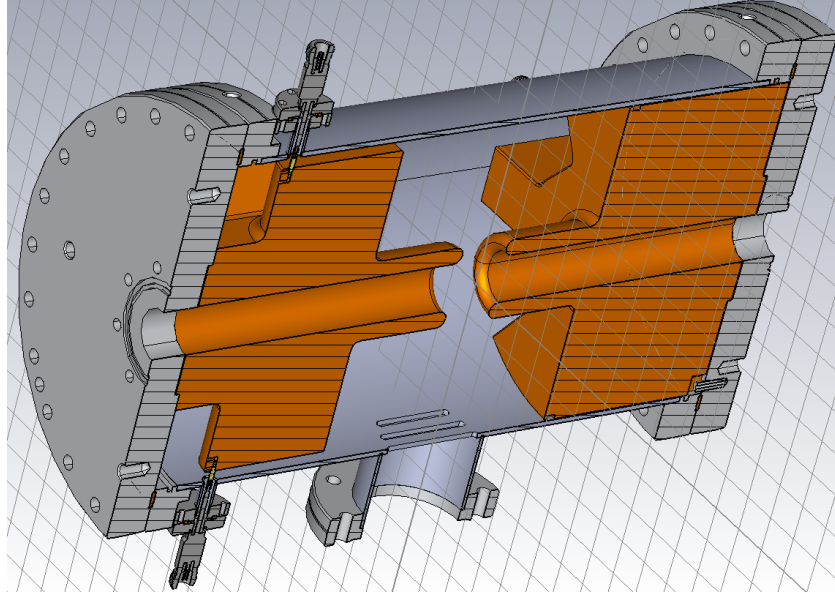


Figure 12: A 3D model of the assembled cavity.

the outer steel pipe. Proper electrical contact between the steel pipe and the copper bodies are provided by silver plated CuBe contact springs as in the ELSA design [15], where the springs are placed in grooves in the copper body as shown in Figure 13 (a). Electrical contact between the inner conductor of the coaxial feedthrough and the copper body is provided by gold plated socket connectors that are screwed to the latter as seen in Figure 13 (b). These socket connectors are the same type as the female inner pin at the N-type connector of the feedthroughs. The cavity is manufactured by FMB Berlin [12].

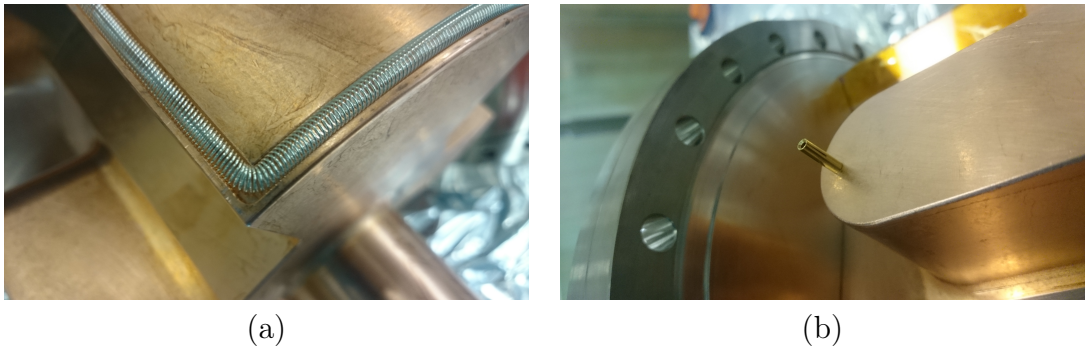


Figure 13: (a) shows the silver plated contact springs that provide electrical contact between the copper bodies and the steel pipe. (b) shows the gold plated socket connectors where the inner conductor of the feedthroughs are inserted.

4.2 Cavity Requirements

The first step when designing the cavity is to determine its center frequency f_c and its bandwidth (BW). As explained in Section 2.3.1, the minimum required BW in order to suppress all CBMIs is $f_{\text{RF}}/2 = 50$ MHz if f_c is chosen so that $f_c = f_{\text{RF}}(1/4 + n/2)$, $n \in \mathbb{N}$. f_c in similar cavities might vary between 900 MHz [29] and 1900 MHz [18], and is often carefully chosen and optimized for the conditions at the facility where it is installed. Choosing a higher f_c has several advantages such as a more compact cavity and a higher achievable shunt impedance, $R_{||}$. Another advantage with a higher f_c is that all the potentially harmful HOMs are shifted upwards as well. The most important figure of merit when designing a cavity is the longitudinal shunt impedance, $R_{||}$, which is given by

$$R_{||} = \frac{V_{||}V_{||}^*}{2P} \quad (4.1)$$

where P is the input power, $V_{||}$ is the gap voltage seen by an ultra-relativistic particle, and $V_{||}^*$ its complex conjugate. $V_{||}$ is obtained from the longitudinal electric field along the center of the cavity $E_z(z)$, and is given by (4.2) where $k = \omega/c_0$ is the wavenumber and φ an arbitrary phase. Here, the integral length L is large enough so that $E_z(|z| > L) \approx 0$ ¹.

$$V_{||} = \int_{-L}^L E_z(z) e^{j(kz+\varphi)} dz \quad (4.2)$$

It is also useful to define the geometrical factor ($R_{||}/Q_0$) in order to compare the performance of different geometries without taking the conductivity of the materials and external loading into account. $Q_0 = \omega W/P$ is the unloaded quality factor, where W is the total stored electromagnetic energy inside the structure.

When selecting f_c , one also has to consider the relatively long bunches at MAX IV. Currently, both rings have double RF systems, where the accelerating cavities operate at $f_{\text{RF}} = 100$ MHz and the passive Landau cavities operate at $3 \cdot f_{\text{RF}}$. With optimum bunch lengthening, each bunch has a quartic (super Gaussian) distribution with $\sigma = 187$ ps \equiv 56 mm (FWHM = 562 ps \equiv 169 mm). There are future plans to operate with a triple RF system in the 3 GeV ring in order to increase the bunch lengthening further by adding 5:th harmonic cavities as well. Figure 14 shows the normalized charge distribution of a single bunch in TD, $\lambda(t)$, and in FD, $\lambda(\omega)$, during ideal bunch lengthening with a double and a triple RF system². The issue with the long bunches is that the head of the bunch obtains a kick with the opposite direction compared to its tail if f_c is chosen too high due to the time varying fields. To illustrate this, assume that each bunch has a normalized spatial distribution $\lambda_z(z)$ so that $\int \lambda_z(z) dz = 1$, and $\lambda_z(c_0 t) c_0 = \lambda(t)$. Then, a single electron at position z'

¹Note that the gap voltage is sometimes defined as $\int |E_z(z)| dz$ in the literature. Thus, with that definition, $V_{||}$ is a real value and the transit time of the particle is not taken into account.

²TD data provided by Pedro F. Tavares

will experience the voltage $V_e(z')$

$$V_e(z') = \int_{-L}^L E_z(z) e^{j(k(z-z')+\varphi)} dz = V_{||} e^{-jkz'} \quad (4.3)$$

The average voltage gain over the normalized electron bunch V_{avg} is then

$$\begin{aligned} V_{\text{avg}} &= \int_{-L}^L \lambda_z(z') V_e(z') dz' = V_{||} \int_{-L}^L \lambda_z(z') e^{-jkz'} dz' \\ &= V_{||} \int_{-L/c_0}^{L/c_0} \lambda_z(c_0 t') e^{-j\omega t'} c_0 dt' = V_{||} \lambda(\omega) \end{aligned} \quad (4.4)$$

Note that the Fourier transform of $\lambda(t)$ in (4.4) is only a valid approximation when $\lambda(z) \approx 0$ for $|z| > L$. Consequently, one can define the effective geometrical factor $(R_{||}/Q_0)_{\text{eff}}$ as

$$(R_{||}/Q_0)_{\text{eff}} = \frac{V_{\text{avg}} V_{\text{avg}}^*}{2P_{\text{rms}}} \frac{1}{Q_0} = (R_{||}/Q_0) \cdot |\lambda(\omega)|^2 = \frac{2}{\omega} \kappa_{||,1} \quad (4.5)$$

where $\kappa_{||,1}$ is the (longitudinal) modal loss factor of the fundamental mode ($n = 1$ in (4.11)). Note that $(R_{||}/Q_0)_{\text{eff}} \rightarrow R_{||}/Q_0$ when $\lambda(t) \rightarrow \delta(t)$, where $\delta(t)$ is the Dirac delta distribution. As seen in Figure 14 (b), we have to select an f_c that is considerable lower than for other similar cavities in order not to lose the kick efficiency when operating with a triple RF system. A good compromise between a compact cavity geometry and fairly high $(R_{||}/Q_0)_{\text{eff}}$ is to set $f_c = 625$ MHz. Here, $|\lambda(f_c = 625 \text{ MHz})|$ is 0.77 and 0.40 for a double and for a triple RF system, respectively. This frequency is also well within the terrestrial UHF band which makes it easier to find suitable commercial RF amplifiers and other high-power RF component for the distribution network.

4.3 Cavity Body

Once f_c was decided, the geometry of the unloaded (no attached WGs) cavity body was designed. Some mechanical restrictions were set on the cavity body. The first restriction was that the cavity beam pipe should have a circular cross section with a radius of 15 mm which is the same cross section as the neighbouring vacuum chambers. Secondly, the initial plan was to manufacture the cavity in-house, and the restriction was that the largest allowed inner radius of the cavity was 103.5 mm in order for the metal pieces to fit the milling machine. The goal is to maximize $R_{||}/Q_0$ of the fundamental mode and at the same time to minimize $R_{||}/Q_0$ of the first longitudinal HOMs. By minimizing $R_{||}/Q_0$ of the HOMs, their coupling to the beam is decreased. The radius of a simple pillbox cavity with $f_c = 625$ MHz is $(c_0 \eta_{0,1})/(2\pi f_c) = 184$ mm which is larger than the design restriction of 103.5 mm. Therefore, f_c is shifted with a coaxially loaded structure. In order to simplify the manufacturing process, simple nose cones are added. Thus, no mushroom structures (as in the main and Landau cavities) are investigated. The nose cones also

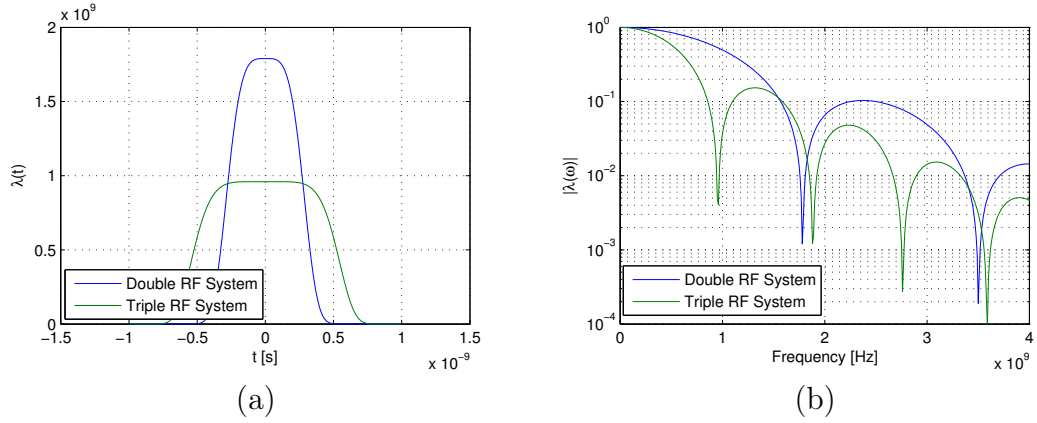


Figure 14: (a) shows the normalized charge distribution of a bunch in TD, $\lambda(t)$, and (b) shows the distribution in FD, $|\lambda(\omega)|$. The charge distributions are for a double (100 MHz + 300 MHz) and for a triple (100 MHz + 300 MHz + 500 MHz) RF system during ideal bunch lengthening.

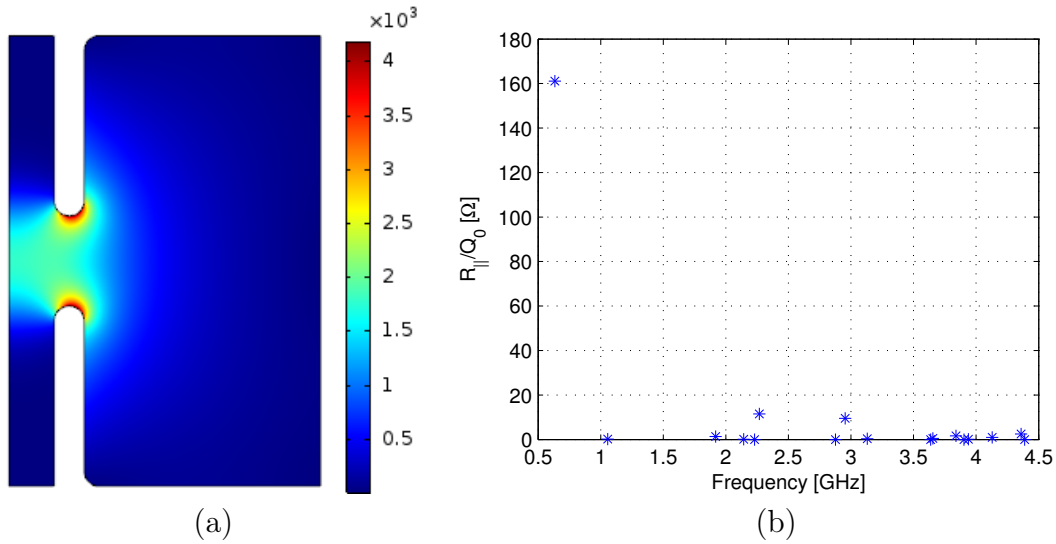


Figure 15: (a) shows $|\mathbf{E}(\mathbf{r})|$ of the optimized rotation-symmetrical fundamental mode of the unloaded cavity in COMSOL. The scale of $|\mathbf{E}(\mathbf{r})|$ is arbitrary. (b) shows $R_{||}/Q_0$ of the rotation-symmetrical eigenmodes in the same cavity up to 4.5 GHz.

increase the field focusing and thereby increase $R_{||}/Q_0$. The optimization of the 2D rotation-symmetrical cavity body was performed in a MATLAB script with livelink to COMSOL. Note that the geometry of the cavity has to be slightly modified when the WGs are added since they perturb the fields and thereby shift f_c . The fundamental mode of the optimized unloaded cavity has $R_{||}/Q_0 = 162 \Omega$. Figure 15 (a) shows $|\mathbf{E}(\mathbf{r})|$ of the fundamental mode obtained in COMSOL, and Figure 15 (b) shows $R_{||}/Q_0$ of the rotation-symmetrical eigenmodes up to 4.5 GHz. As a comparison, $R_{||}/Q_0$ of the main and Landau cavities are 86Ω and 133Ω , respectively.

4.4 Cavity Matching

As mentioned above, the required BW of the cavity is 50 MHz, centred around f_c . Here, the BW is defined as the 3 dB BW of the common-mode transmission coefficient S_{cc21} (see below). Note that it would also be possible to define the BW from $R_{||}(\omega)$. However, a somewhat larger BW of 70 MHz is chosen, and the cavity is matched so that the 3 dB limits of S_{cc21} are located at 590 MHz and 660 MHz. Of course, a larger BW lowers the peak $R_{||}$, but it results in a better gain flatness and makes the mechanical tolerances less critical in the manufacturing process. The required BW gives a loaded quality factor of $Q_L = f_c/f_{BW} = 8.9$. The BW is simply increased by increasing the power losses in the cavity system, and this is achieved by adding four ridged WGs to the pillbox cavity as seen in Figure 16. The WGs are optimized to have a good transmission to the cavity in a span from ≈ 500 MHz to ≈ 2500 MHz. The large BW of the WGs also ensures that the first HOMs are damped, which makes them less likely to drive any CBMIs. Each WG is terminated with 50Ω via a coax-to-waveguide transition. The two pair of WGs at each side are rotated 90° relative to each other in order to make the fields of the fundamental mode as symmetric as possible. This orientation also improves the damping of dipole HOMs. Consequently, almost all the power delivered to the cavity by the amplifier and by the beam is lost in the external loads, and this also removes the need for water cooling of the cavity. No tuning mechanism is added to the cavity since the mechanical tolerances in the manufacturing process are relatively low due to the rather large BW.

The fundamental mode is excited when the two WGs at the upstream (or downstream) end are driven with the same amplitudes and phases (common-mode), while the other two WGs are terminated as shown in the driving scheme in Figure 17. The amplifiers that feed the two WGs are protected via circulators from reflected waves and from backward travelling waves that are excited in the cavity by the beam itself. Figure 18 shows the S-parameters obtained in COMSOL where the physical ports 1 and 3 in Figure 17 form the logical mixed-mode port 1, and the physical ports 2 and 4 form the logical mixed-mode port 2. As seen $S_{cc11}(f = 590 \text{ MHz}) \approx S_{cc11}(f = 660 \text{ MHz}) \approx -3 \text{ dB}$. Also note that f_c is shifted to 621 MHz in order to keep the BW in the 590 - 660 MHz range.

One can represent the cavity with the two identical (but orthogonal) upstream and downstream WG pairs as the resonant circuit in Figure 20 (a), where the resonance frequency is given by $\omega_c^2 = (LC)^{-1}$. Here, each WG pair is modelled as a

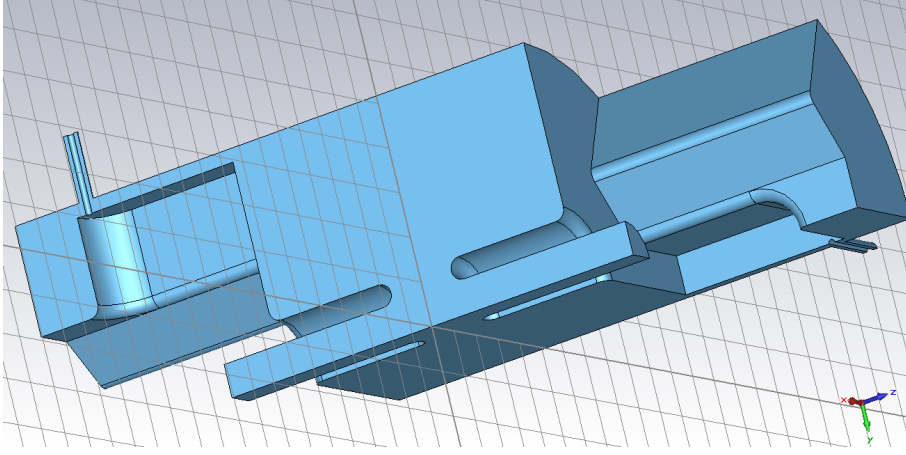


Figure 16: 1/4 of the cavity vacuum body when the four ridged WGs are added.

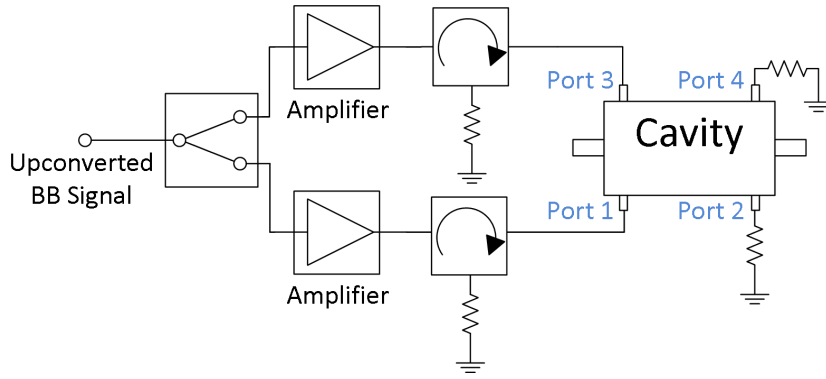


Figure 17: The driving scheme of the cavity.

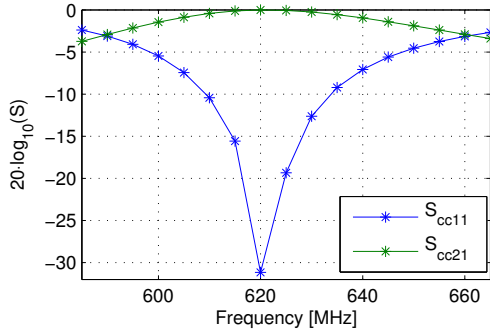


Figure 18: The common-mode S-parameters of the cavity.

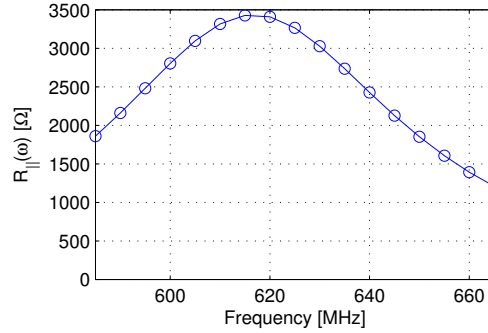


Figure 19: $R_{||}(\omega)$ of the cavity around its span of operation.

coupler transformer with the turns ratio $1 : n$. Each transformer is terminated with a load with the impedance $Z_0 = 50 \, \Omega$ via a transmission line with a characteristic impedance of Z_0 . The RF source corresponds to the drive amplifiers. The cavity

itself corresponds to the RLC circuit in the middle, with the circuit shunt resistance $R \gg Z_0$. The circuit in Figure 20 (a) can be transformed into the RF source circuit, as in Figure 20 (b). Now, assume that a voltage $V(t) = \hat{V} \cos(\omega_c t)$ is applied over the circuit, then the total energy that is stored in the system is $W = n^2 C \hat{V}^2 / 2$. The unloaded quality factor of the cavity itself becomes $Q_0 = \omega_c W / P_c = \omega_c R C$, where $P_c = n^2 \hat{V}^2 / (2R)$ is the power dissipated in the cavity walls. The quality factors of the two external circuits (the two waveguides) are $Q_{e1} = Q_{e2} = \omega_c W / P_{e1} = \omega_c n^2 Z_0 C$, where $P_{e1} = \hat{V}^2 / (2Z_0)$ is the power dissipated in the circuit of the RF source. The loaded Q factor, Q_L , is then obtained as

$$\frac{1}{Q_L} = \frac{1}{Q_0} + \frac{1}{Q_{e1}} + \frac{1}{Q_{e2}} = \frac{1}{Q_0} + \frac{2}{Q_{e1}} \quad (4.6)$$

If the interior material of the unloaded cavity is made of copper or SS316L, Q_0 is 16808 and 2514, respectively. Since $Q_L = 8.9 \ll Q_0$, we have that $Q_L \approx Q_{e1}/2$, thus the choice of material has an insignificant effect on the cavity BW.

One drawback with the circuit model described above is that it is only accurate for a cavity system with high Q_L where it is assumed that the coupler(s) have the same transmission/reflection coefficients to the cavity within the narrow BW of the resonator. This is not true in the case of overloaded cavity which can be seen in the slightly asymmetrical S-parameters in the 3 dB BW span around f_c in Figure 18. Despite this, the circuit model is an intuitive way to understand the overloaded cavity, and it provides a good approximation of the power dissipation in the cavity system.

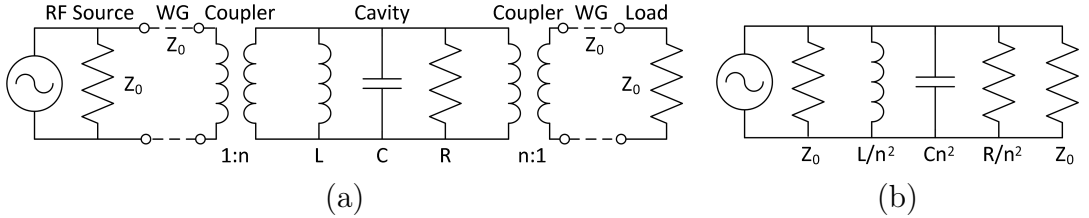


Figure 20: (a) shows an equivalent circuit model of the cavity with two identical couplers, where the first one is connected to the RF source and the second to an external load. (b) shows the same circuit transformed into the RF source.

The shunt impedance, $R_{||}(\omega) = |V_{||}(\omega)|^2 / (2P_{in}(\omega))$, around the frequency span of operation can be seen in Figure 19. Here, $P_{in}(\omega)$ is the total input power at Port 1 and 3, as shown in Figure 17. $V_{||}(\omega)$ is obtained from $E_z(z, \omega)$ in the 3D model. As seen, $R_{||}(\omega)$ is lower in the upper half of the operational span than in the lower half. This is mainly because the transit time factor decreases with frequency. It would be possible to make the shunt impedance more symmetrical in the span of operation by shifting the port matching to a higher frequency, but it was decided to keep the -3 dB S-parameter BW as it is.

The shunt impedance at the resonance frequency f_c can also be roughly estimated from the circuit model. If we feed the cavity as in Figure 17, almost all the power

is lost in the two loads that are connected to Port 2 and 4 which correspond to the right Z_0 resistor in Figure 20 (b). Thus, with this set-up, the quality factor of the complete system is $\approx Q_{e2}$. By using $R_{||}/Q_0 = 162 \, \Omega$ obtained from the unloaded cavity in the 2D simulations, $R_{||}(\omega_c)$ can be estimated as in (4.7). The maximum value of $R_{||}(\omega)$ in Figure 19 is $\approx 3.4 \, \text{k}\Omega$.

$$R_{||}(\omega_c) \approx (R_{||}/Q_0) \cdot Q_{e2} \approx 2.9 \, \text{k}\Omega \quad (4.7)$$

4.5 Wakefields and Heat Load

The wakefields in the structure are simulated in GdfidL [13], where the mesh size and wake length are set to 0.4 mm and 40 m, respectively. Here, the feedthroughs are simulated as simple coaxial waveguides that are terminated with several layers of perfectly matched layers, i.e., the sub components of the feedthroughs are not included. The longitudinal beam impedance $Z_{||}(\omega)$ is shown in Figures 21-22, while the transverse beam impedance $Z_{\perp}(\omega)$ is shown in Figure 24. When inspecting $\text{Re}(Z_{||}(\omega))$ in Figure 21, one can distinguish three different regions. In the first region, where $f \lesssim 3 \, \text{GHz}$, the eigenmodes are heavily damped by the WGs, and they are quite wideband. In the region where $3 \, \text{GHz} \lesssim f \lesssim 8 \, \text{GHz}$, the eigenmodes do not couple as much to the WGs due to the finite BW of the WGs and/or due to the fact that these eigenmodes do not have field distributions that couple to the geometrical cross sections of the WGs. Therefore, the eigenmodes in this regions are narrowbanded compared to those in the first region. The broad-band impedance region appears when $8 \, \text{GHz} \lesssim f$ which is above the TM_{01} cut-off frequency of the beam pipe which is 7.6 GHz. Here, the longitudinal modes with field components in the beam pipe center are not trapped, but are propagating or semi-propagating.

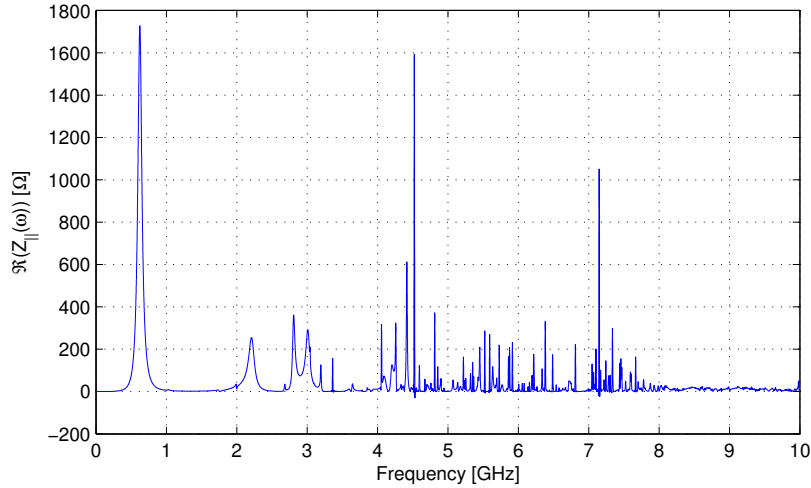


Figure 21: $\text{Re}(Z_{||}(\omega))$ of the cavity up to 10 GHz.

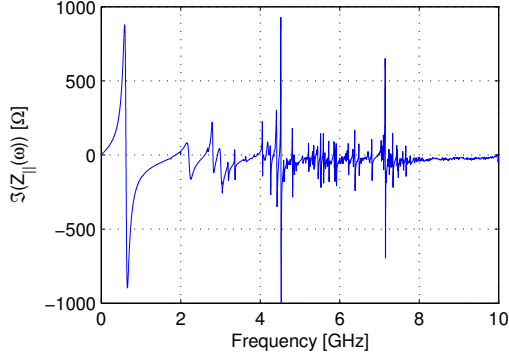


Figure 22: $\text{Im}(Z_{\parallel}(\omega))$ of the cavity up to 10 GHz.

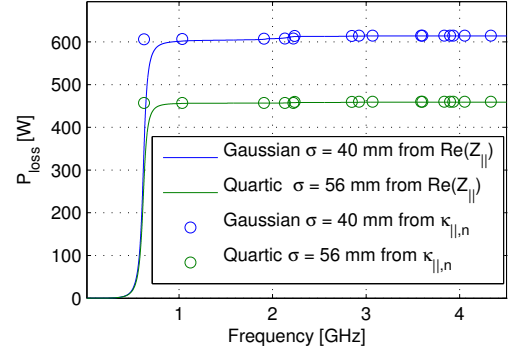


Figure 23: $\int_0^\omega dP_{\text{loss}}(\omega') d\omega'$ calculated from κ_{\parallel} in (4.10) and from $\kappa_{\parallel,n}$ in (4.12) for two different bunch profiles at 500 mA.

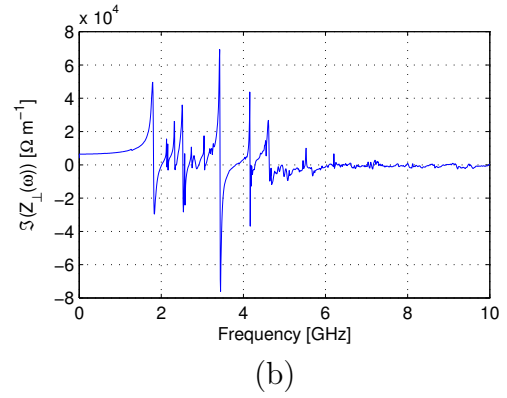
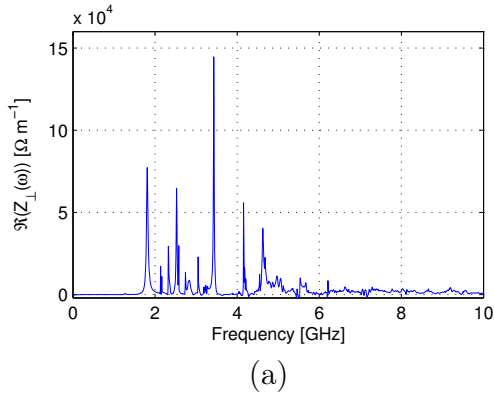


Figure 24: $\text{Re}(Z_{\perp}(\omega))$ (a) and $\text{Im}(Z_{\perp}(\omega))$ (b) of the cavity up to 10 GHz.

Since the fundamental mode has a quite high $(R_{||}/Q_0)_{\text{eff}}$, the beam induced power, P_{loss} , in the cavity is considerable. However, as explained above, almost all beam induced power dissipates in the external loads, which is shown in (4.8). P_{loss} is obtained from the longitudinal loss factor $\kappa_{||}$ as in (4.9)-(4.10), where I_0 is the total beam current. Note that (4.10) is only valid for a uniform filling pattern and has to be modified if other filling patterns are used. A conservative way to estimate P_{loss} is to calculate it for Gaussian bunches with $\sigma = 40$ mm at the maximum design current of 500 mA. Table 3 shows $\kappa_{||}$ and P_{loss} obtained from (4.9)-(4.10) for Gaussian bunches and for the quartic $\sigma = 56$ mm bunches (double RF system). Unlike the striplines, the cavity is a non-directional device, and P_{loss} is distributed almost equally among the four external loads. These loads have to be able to handle P_{loss} plus the additional power from by the feedback system.

$$P_{\text{loss}} = P_c + P_{e1} + P_{e2} = P_c(1 + 2Q_0/Q_{e1}) \Rightarrow P_c = P_{\text{loss}}/(1 + 2Q_0/Q_{e1}) \quad (4.8)$$

$$\kappa_{||} = \frac{1}{\pi} \int_0^\infty \text{Re}(Z_{||}(\omega)) \lambda(\omega) \lambda^*(\omega) d\omega \quad (4.9)$$

$$P_{\text{loss}} = \frac{I_0^2}{f_{\text{RF}}} \kappa_{||} \quad (4.10)$$

P_{loss} can also be estimated from the modal loss factors $\kappa_{||,n}$ as seen from (4.11)-(4.12). Here, $\omega_{c,n}$ and $(R_{||}/Q_0)_n$ are the angular resonance frequency and the geometrical factor of the n :th eigenmode, respectively. This estimation is of course more accurate when the modes are more narrow (higher Q) since the variations in $\lambda(\omega)$ are smaller over the BW of the modes.

$$\kappa_{||,n} = \frac{\omega_{c,n}}{2} \left(\frac{R_{||}}{Q_0} \right)_n \lambda(\omega_{c,n}) \lambda^*(\omega_{c,n}) \quad (4.11)$$

$$P_{\text{loss}} = \frac{I_0^2}{f_{\text{RF}}} \sum_{n=1}^\infty \kappa_{||,n} \quad (4.12)$$

To show how P_{loss} is distributed among the eigenmodes, $\int_0^\omega dP_{\text{loss}}(\omega') d\omega'$ obtained from (4.10) and (4.12) is plotted in Figure 23. Here, the modal loss factors are obtained directly from the rotational-symmetric 2D simulations of the unloaded cavity. Even though the WGs have shifted the eigenmodes and perturbed the fields, there is a quite good agreement between the two methods. It is easy to see that almost all the beam induced power couples to the fundamental mode.

In the calculations of P_{loss} above, it is assumed that the power lost by the beam is incoherent, i.e., that there is no coherent multi-turn wakefield superposition. Such coherent power loss appears when the multi-turn spectrum of the beam coincides with peaks in $\text{Re}(Z_{||}(\omega))$ that are caused by eigenmodes with considerable Q -factors. Thus, with a uniform fill pattern, this occurs if the spectrum of the eigenmodes overlap with any harmonic of f_{RF} . As seen in Figure 21, the lower part of the beam

Guassian $\sigma = 40$ mm		Quartic $\sigma = 56$ mm	
$\kappa_{ }$ [mV/pC]	P_{loss} [W]	$\kappa_{ }$ [mV/pC]	P_{loss} [W]
245	614	183	457

Table 3: $\kappa_{||}$ and P_{loss} in the cavity obtained from (4.9)-(4.10) for two different bunch profiles. P_{loss} is obtained for a uniform filling pattern at a total beam current of 500 mA.

spectrum of the fundamental mode overlaps with $6 \cdot f_{\text{RF}}$ due to the high BW, but a Q_L of 8.9 is considered too low to cause any notable coherent power loss [24]. As a comparison, the fall time of the voltage in the eigenmode is $\tau_f = 2Q_L/\omega_c \approx 4.5$ ns, while the bunch separation is 10 ns. Such coherent multi-turn wakefield superposition is by the way the working principle of the passive Landau cavities, but Q_L in those structures is above 10000.

4.6 Vacuum Port

Since the inner volume of the cavity chamber is quite large compared to the cross section of the beam pipe, it was decided to add an ion pump to the design in order to improve the vacuum quality inside the cavity and in its surrounding chambers. The pipe that is connecting the ion pump to its CF75 flange is welded to the mid part of the cavity lateral surface. In order to perturb the cavity fields as little as possible, the pumping slits are milled so that they are oriented parallel to the surface currents $\mathbf{J} = \hat{\mathbf{n}} \times \mathbf{H}$. For the TM_{010} mode in a pillbox cavity, \mathbf{J} is oriented in the $\pm z$ direction at the lateral surface. The four WGs do however perturb the fields and add an azimuthal component of \mathbf{J} on the lateral surface, as shown in Figure 25 (a). The slits are therefore milled where J_ϕ is small, which is shown in Figure 25 (b). Simulations show that the introduction of the ion pump has an insignificant effect on the field distribution and on the port matching.

4.7 Measurements

The mixed-mode measurements were performed with a 4-port VNA, and Figure 26 shows the measurement set-up. The port indices correspond to those in the driving scheme in Figure 17. The measured and simulated common-mode S-parameters around the fundamental mode can be seen in Figure 27. The simulation results are here obtained in COMSOL, and the full details of the ceramic feedthroughs are included, unlike the evaluation of S-parameters in Figure 18. Resistive and dielectric losses of the complete cavity are also included in the model. The measured 3 dB BW obtained from S_{cc21} is 74 MHz (590 MHz - 664 MHz), which is acceptable. The main reason why the measured S_{cc11} resonance is wider than the simulated is that the losses in the ceramic feedthroughs are lower in the latter. The interior of the feedthroughs is the same as in the striplines, and the simulations of these components do also underestimate the losses (see Section 3.3), despite using all

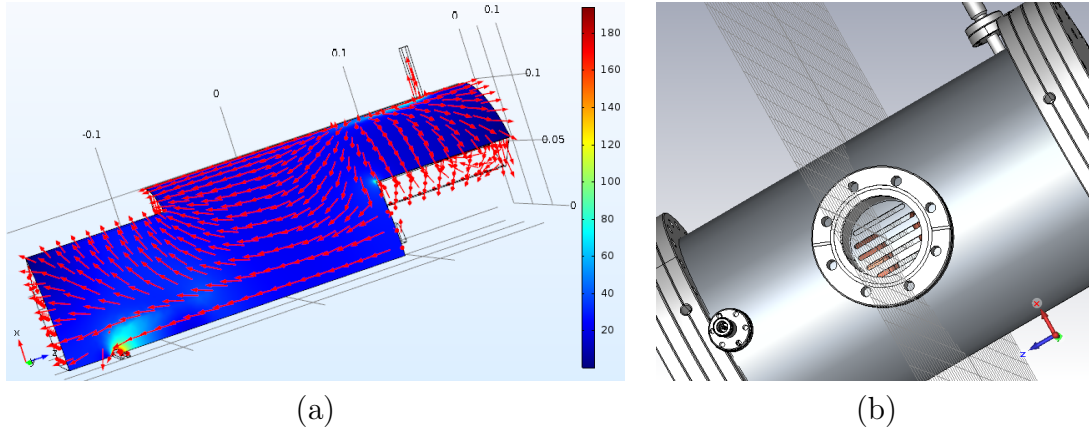


Figure 25: (a) shows the surface currents \mathbf{J} (arrows) and its magnitude $|\mathbf{J}|$ (color scheme) at the cavity lateral surface. (b) shows the pipe that is added for the ion pump and the orientation of the pumping slits at the lateral surface.

the dimensions and material parameters provided by the supplier. The measured resonance frequency of the fundamental mode is $f_c = 621$ MHz, and agrees well with the simulations.

The volume around the feedthroughs and the ridged WGs were considered critical from a tolerance perspective since proper electrical contact here is important for the matching of the cavity. In order to verify the matching of each WG, a single-ended measurement of each port was performed. Here, the reflection parameter of each physical port was measured, while the other three ports were terminated. Figure 28 shows the results and one can see that the matching is slightly different for each port. The variations are acceptable, and no further investigations were made to find if the variations were caused by mechanical variations in the cavity or in the feedthroughs.

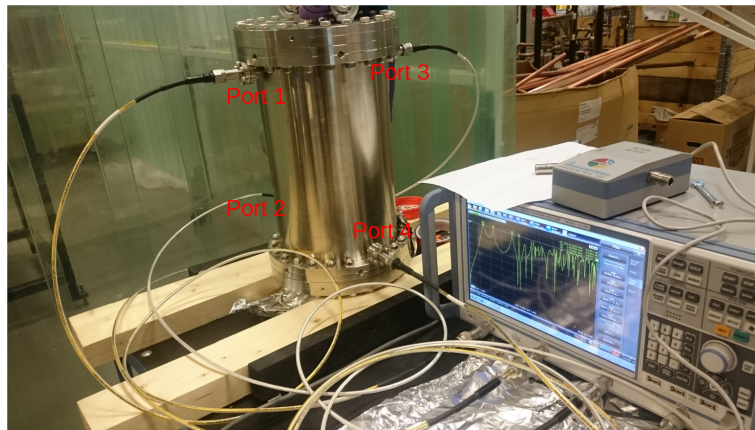


Figure 26: The set-up during the mixed-mode S-parameters measurements of the cavity.

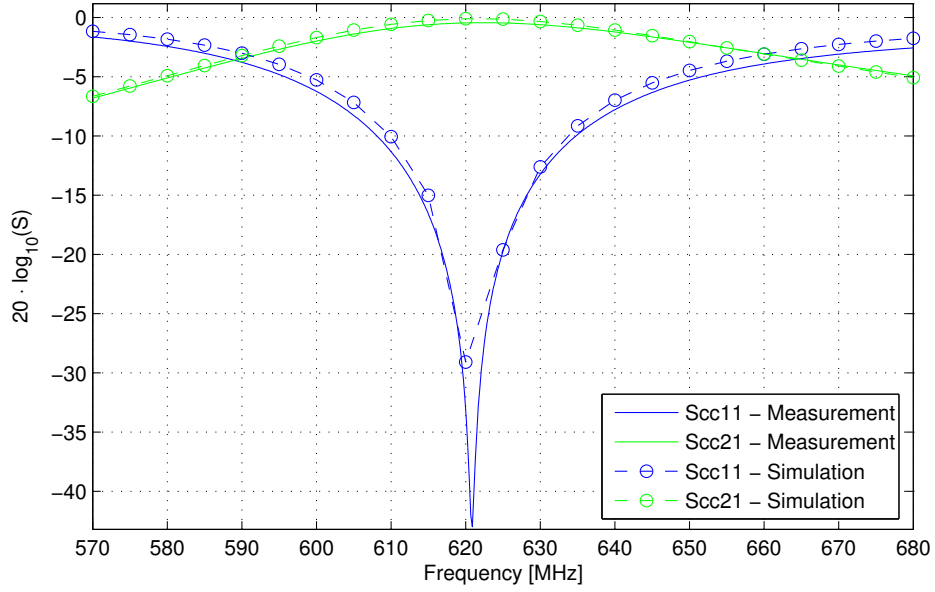


Figure 27: The measured and simulated common-mode S-parameters of the cavity around the fundamental mode.

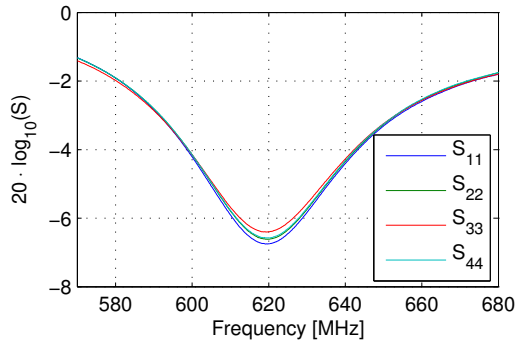


Figure 28: The measured single-ended reflection parameters of the cavity around the fundamental mode.

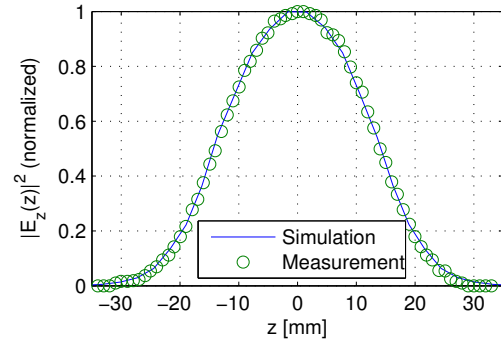


Figure 29: The measured and simulated electric field in the cavity along its center axis ($x = y = 0$).

A bead-pull measurement was also performed to characterize E_z along the cavity center axis. Here, the bead was a steel ball (taken from a ball bearing) with a radius of $a = 4$ mm. The ball was translated along the center axis via a 0.15 mm thick fishing line, and the shift of the resonance frequency was measured from S_{cc11} as the metal ball moved along the cavity. The Slater perturbation theorem describes the shift in resonance frequency when a small volume is removed from a resonance cavity. If the reduced volume is caused by a metallic ball, the relationship between the frequency shift, $\Delta\omega(z)$, and the magnitude of the longitudinal electric field,

Parameter	Measurement	Simulation
f_c	621 MHz	621 MHz
BW (from S_{cc21})	74 MHz	70 MHz
Q_L	8.4	8.9
$R_{ }(f = f_c)$	3.31 k Ω	3.35 k Ω

Table 4: The cavity parameters obtained from the measurements. The results are compared with simulation results obtained in COMSOL, where the resistive and dielectric losses from the cavity walls and from the feedthroughs are included.

$|E_z(z)|$, when the ball is at position z is given by

$$\frac{\Delta\omega(z)}{\omega_c} = -\frac{\epsilon_0\pi a^3}{W}|E_z(z)|^2 \quad (4.13)$$

where ϵ_0 is the permittivity of free space, ω_c the resonance frequency of the unperturbed cavity, and W is the time average of the stored energy inside the cavity [27]. In (4.13), it is assumed that the magnetic field is close to zero and that the derivative \mathbf{E} is small compared to a in the vicinity of the metal ball, which is true in the gap between the nose cones. E_z also extends somewhat into the beam pipes, and the approximation is less accurate here (the beam pipe has a radius of 15 mm), and a larger discrepancy can here be seen in the measurement results. However, the fields are quite low in these regions and contribute little to $R_{||}$. Figure 29 shows the measured and simulated $|E_z(z)|^2$ along the center axis. As seen, there is a good agreement. The voltage gain, $V_{||}$, at the resonance frequency can now be calculated as

$$V_{||} = \int_{-L}^L |E_z(z)|e^{jkz} dz = \sqrt{\frac{W}{\omega_c\epsilon_0\pi a^3}} \int_{-L}^L \sqrt{-\Delta\omega(z)}e^{jkz} dz \quad (4.14)$$

where k is the wavenumber, and $2L$ is the total integration length. The shunt impedance, $R_{||}$, at the resonance frequency can then be obtained as

$$R_{||} = \frac{|V_{||}|^2}{2P} = \frac{Q_L}{\omega_c^2\epsilon_0\pi a^3} \left(\int_{-L}^L \sqrt{-\Delta\omega(z)}e^{jkz} dz \right)^2 \quad (4.15)$$

where P is the total power fed to Port 1 and 3 in common-mode. In (4.15), we are using the relationship between stored energy and power which is $W/P \approx Q_{e2}/\omega_c \approx 2Q_L/\omega_c$ since almost all the input power is dissipating in the terminations at Port 2 and 4 (thus in the second external port as described in Section 4.4). The measurement gives $R_{||}(\omega_c) = 3.31$ k Ω , which is close to the simulated value of 3.35 k Ω (the losses in the metal walls and in this feedthroughs are included in this simulation). The measured and simulated parameters are summarized in Table 4.

5 The BBB Feedback System

As mentioned, the focus of this report is on the BBB feedback system in the 3 GeV ring, and Section 5.1 describes the layout of that system. A short summary on the

current status of the BBB feedback system in the 1.5 GeV ring is given in Section 5.2.

5.1 BBB Feedback in the 3 GeV Ring

The commissioning of the BBB feedback system in the 3 GeV started in the beginning of 2016. This far, it has been possible to keep the beam stable in all three planes at beam currents that are above 100 mA. The largest challenge has been to keep the beam stable in the longitudinal plane. As mentioned, the longitudinal feedback has been provided by the striplines. It will hopefully be possible to reach the maximum design current of 500 mA once the overloaded cavity is installed after the 2017 summer shut-down. At higher currents, we can also tune in the Landau cavities which would suppress the CBMs further due to the increased bunch lengthening and Landau damping.

5.1.1 Front-End

The first part of the BBB feedback system is the detector-end, also known as the front-end. The beam signal is here monitored at the standard 4-button BPM chamber, depicted in Figure 30 (a). In order to create the horizontal and vertical differential, as well as the sum signal from the four buttons, a hybrid network was constructed which can be seen in Figure 30 (b). This network is basically the same as the "receiving network" described in [20], except there are no electromechanical switches. Figure 5 shows the phase and amplitude balance of the hybrid network obtained from its S-parameters.

BPM Port, x	Horizontal		Vertical		Sum	
	$20 \cdot \log_{10}(S_{5x})$	$\arg(S_{5x})$	$20 \cdot \log_{10}(S_{6x})$	$\arg(S_{6x})$	$20 \cdot \log_{10}(S_{7x})$	$\arg(S_{7x})$
1	-9.92	56.1°	-9.54	-123.2°	-9.65	56.0°
2	-9.77	-124.9°	-9.64	-122.4°	-9.77	56.7°
3	-9.71	-123.4°	-9.85	60.8°	-9.65	58.4°
4	-9.53	57.8°	-9.89	63.4°	-9.69	60.7°

Table 5: The measured magnitudes and phases of the hybrid network at 1500 MHz. The indices of the ports are shown in green text in Figure 30 (b). Note that the front-end frequency was later changed from 1500 MHz to 1000 MHz.

The input signals to the signal processing units (see Section 5.1.2) must be in baseband (BB), thus in the 0 - 50 MHz range. Therefore, the wideband signals delivered from the hybrid network have to be downconverted to that span. This is done by heterodyning the BPM signals together with a harmonic of the main RF frequency in a front-end unit, as illustrated in Figure 31. The wideband BPM signal is first filtered in a band-pass filter so that its frequency span is in the 950-1050 MHz range, and then mixed with the 10th RF harmonic. The signal at the mixer RF input (see green text in Figure 31) can be approximated as $v_R(t) = A(t) \cos(10\omega_{RF}t + \phi(t))$, where $A(t)$ is an amplitude function which mainly depends on the transverse motion

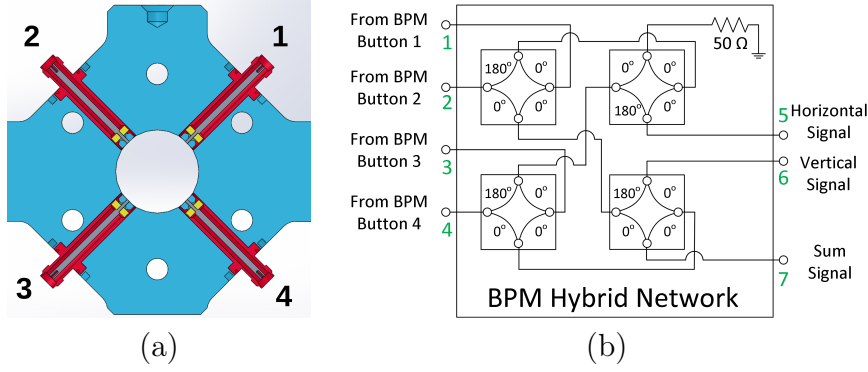


Figure 30: (a) shows a 2D cross section of the BPM chamber and the indices of the four buttons. (b) shows a circuit diagram of the hybrid network where the horizontal, vertical, and sum signals are created.

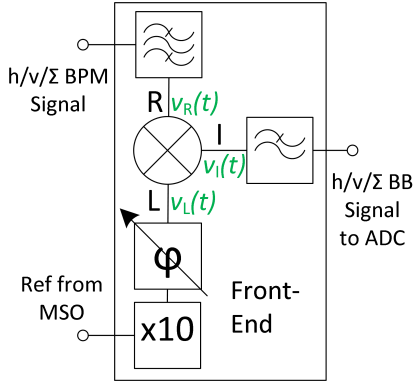


Figure 31: A simplified block diagram of a front-end.

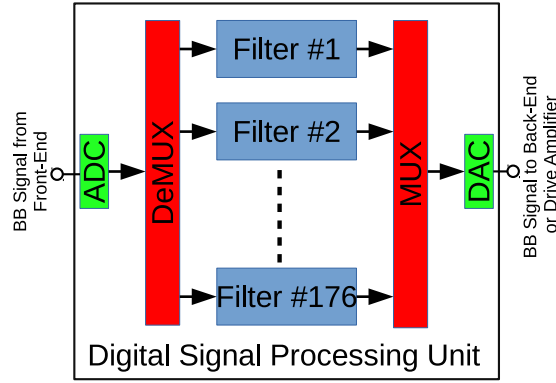


Figure 32: A simplified block diagram of a digital signal processing unit.

of the beam, and $\phi(t)$ is a phase function which is caused by longitudinal bunch oscillations. The signal at the LO input is $v_L(t) = \cos(10\omega_{RF}t + \varphi_0)$, where φ_0 is a phase constant that is set by the phase shifter in Figure 31.

If we are monitoring the horizontal, or vertical differential signal, the amplitude is proportional to the beam displacement in the corresponding plane. If we set $\varphi_0 = 0$, the output signal at the IF port, $v_I(t) = v_R(t)v_L(t)$, becomes

$$v_I(t) = \frac{1}{2}A(t)\{\cos(\phi(t)) + \cos(20\omega_{RF}t + \phi(t))\} \approx \frac{1}{2}A(t)\{1 + \cos(20\omega_{RF}t + \phi(t))\} \quad (5.1)$$

Here, it is assumed that $\phi(t) \ll 1$, thus the beam is stable in the longitudinal plane. The second high-frequency term is then removed by the low-pass filter (see Figure 31), and we see that the output signal of the front-end is proportional to the amplitude of the transverse motion $A(t)$. Signal detection in the horizontal and vertical planes are therefore known as amplitude detection.

When we monitor the longitudinal plane, the sum signal from the hybrid network is used. This signal is not sensitive to transverse beam oscillations, which makes the

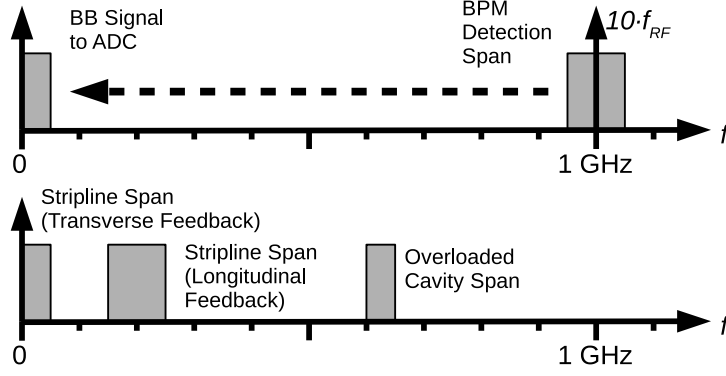


Figure 33: The heterodyning in the front-end (upper), and the span of the feedback signals that are applied to the striplines and to the cavity (lower).

approximation $A(t) = A_0$ relevant, where A_0 is a constant. By setting $\varphi_0 = -\pi/2$, the voltage $v_I(t) = v_R(t)v_L(t)$, becomes

$$v_I(t) = \frac{1}{2}A_0\{\sin(\phi(t)) + \sin(20\omega_{RF}t + \phi(t))\} \approx \frac{1}{2}A_0\{\phi(t) + \sin(20\omega_{RF}t + \phi(t))\} \quad (5.2)$$

Again, the second term is removed by the low-pass filter, and the front-end output signal is therefore proportional to $\phi(t)$. Signal detection in the longitudinal plane is therefore known as phase detection. Note that it is assumed in (5.1)-(5.2) that the mixers are ideal and that they are operating in their linear region.

Figure 33 (upper) shows how the detected BPM signals around $10 \cdot f_{RF}$ are downconverted to BB. A commercial front-end unit delivered by Dimtel [11] is used, and this unit has three separated front-end channels, one for each plane. The Dimtel front-end unit also contains a back-end that will be used for upconverting the BB feedback signal for the overloaded cavity (see Section 5.1.3).

5.1.2 Signal Processing Units

The BBB feedback system is equipped with iGp12 FPGA based signal processing units delivered by Dimtel. Each plane requires its own unit. The three iGp12 units for the 3 GeV ring can be seen in Figure 38.

The signal processing chain consists of a high-speed 12-bit ADC, an FPGA, and a high-speed DAC. The ADC is clocked by f_{RF} , and it samples the turn-by-turn BB signal from the front-end (see Section 5.1.1) of each single bunch. Note that the synchrotron frequency is much lower than the betatron frequencies, so downsampling has to be used in the longitudinal plane. The sampled signal is then demultiplexed into 176 channels (one for each bunch), where each channel is processed with an adjustable digital FIR (Finite Impulse Response) filter. The digital filters are described in detail in [30], and they determine the correction signal (amplitude and

phase) for each bunch. Finally, the correction signals from each channel are multiplexed to a DAC that is also clocked by f_{RF} . The analogue correction signal is then amplified and sent to an actuator (via a back-end if needed, as described in Section 5.1.3). Figure 32 shows a simplified block diagram of a digital signal processing unit.

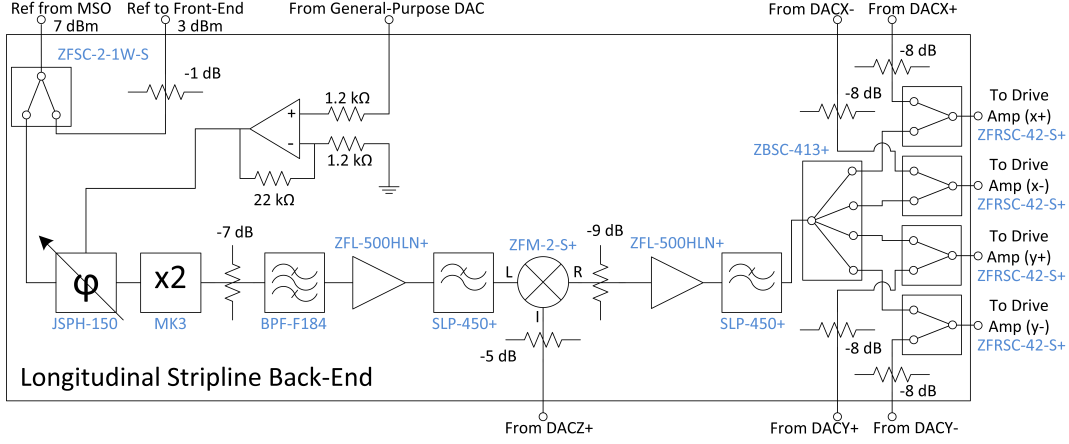


Figure 34: The circuit diagram of the longitudinal stripline back-end. All part numbers are from the Mini-Circuits' catalogue.

The FPGA also has integrated data acquisition memories which makes it possible to analyse the turn-by-turn data (see Section 6.1). Each unit also contains an integrated Linux based computer that controls the FPGA and provides the communication with the outside world via ethernet. The controls are performed via EPICS, and an EPICS-to-Tango gateway makes it possible to control the units via the MAX IV control system.

5.1.3 Back-End

The BB DAC output signals from the three iGp units are differential (each unit has two output ports, with the opposite signal polarity relative to each other). They are named DAC(X/Y/Z)(+/-) depending on which plane, (X/Y/Z), and which polarity, (+/-). The striplines have high transverse shunt impedances, $R_{\perp}(\omega)$, in the 0-50 MHz BB span (see Figure 9), and the transverse feedback signals, DAC(X/Y)(+/-), can therefore be fed directly to the striplines in differential-mode via drive amplifiers.

$R_{\parallel}(\omega)$ is however weak in the BB span, and the DACZ+ signal must therefore be upconverted to a span where $R_{\parallel}(\omega)$ is higher (DACZ- is not needed since the striplines are fed in common-mode when applying longitudinal feedback). A back-end that upconverts the DACZ+ signal to the $f = (2 \pm 0.5)f_{RF}$ range with heterodyning was therefore constructed. Figure 34 shows a block diagram of the longitudinal stripline back-end, and Figure 35 shows the components assembled in a standard 19" rack case. The heterodyning occurs in a mixer where the BB signal is mixed with the second harmonic of f_{RF} . $2 \cdot f_{RF}$ is generated in a frequency doubler, and its phase is adjusted by a voltage controlled phase shifter. The control signal

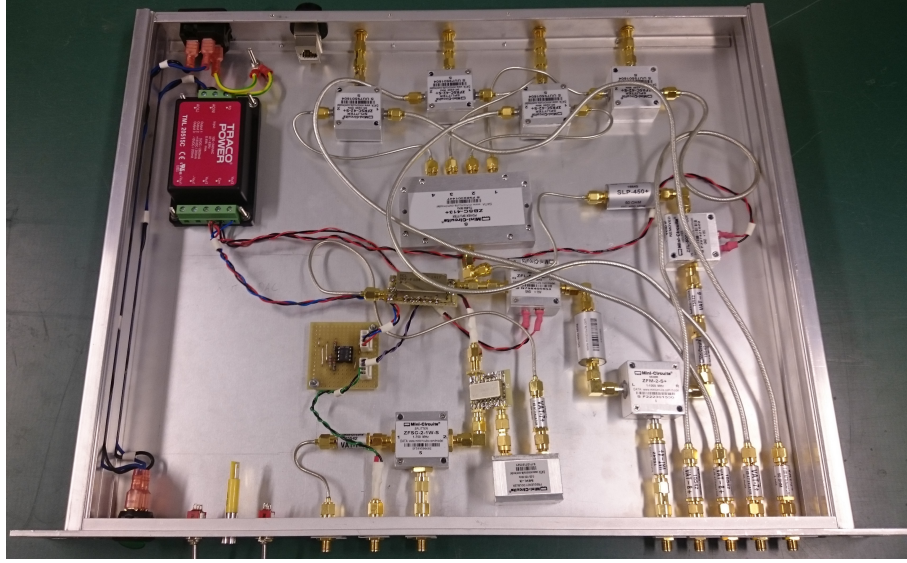


Figure 35: The longitudinal stripline back-end assembled inside a standard 19" rack case.

to the phase shifter is provided by a channel from the general-purpose DAC of one of the iGp units (this is not the same high-speed DAC that is used to generate the feedback signals). This signal is amplified by an OP amplifier to the phase shifter's operational input range of 0-15 V. The upconverted signal is then split into four signals and fed to the four strips via the amplifiers in common-mode. Before feeding these upconverted signals to the amplifiers, they are combined with the DACX+, DACX-, DACY+, and DACY- signals using four resistive splitters. This is shown in Figure 34, and makes it possible to provide longitudinal and transverse feedback with both striplines simultaneously.

Figure 36 shows the power spectrum of one of the output signals of the longitudinal stripline back-end. Here, a 25 MHz CW signal at the maximum DACZ+ output of +2 dBm is applied, and one can see that the isolation between the 25 MHz sidebands of 200 MHz to the highest unwanted peak is more than 30 dB. These neighbouring peaks are a combination of mixer products and harmonics created in the frequency multiplier and in the amplifiers. Figure 37 shows the two output signals when driving 3 bunches ($3 \cdot 10$ ns). As seen, the rise and fall times at 0 and 30 ns respectively are quite short which ensures good bunch-to-bunch isolation during excitation.

The commissioning of the overloaded cavity will start in the autumn of 2017. The DACZ+ signal will then instead be upconverted to the 600-650 MHz range in the Dimtel front/back-end unit. Figure 33 (lower) shows the feedback spans that are applied to the overloaded cavity and to the two striplines when they are operating as transverse and longitudinal actuators.

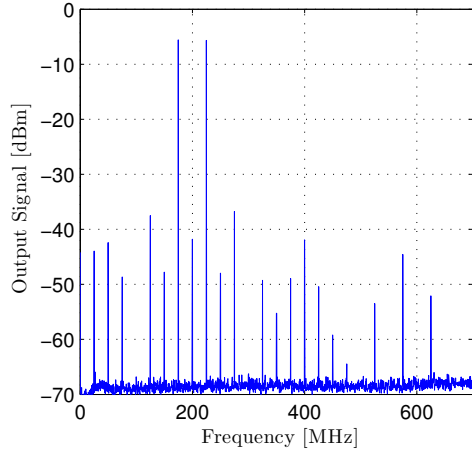


Figure 36: The power spectrum of one of the output signals from the longitudinal stripline back-end measured with a spectrum analyser. Here, a +2 dBm 25 MHz CW signal from DACZ+ is applied.

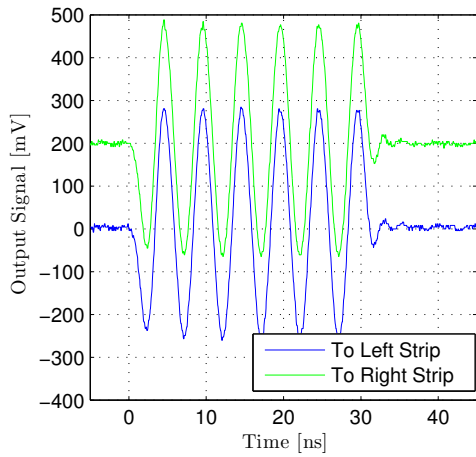


Figure 37: The two output signals to the horizontal stripline from the longitudinal stripline back-end when driving 3 bunches with a 1 kHz signal from DACZ+. The vertical offset of the green curve is 200 mV.

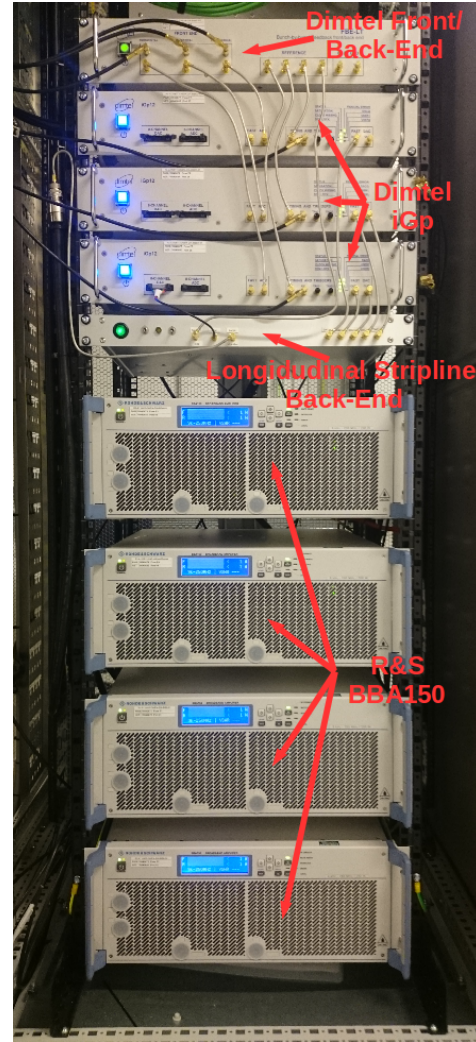


Figure 38: The BBB electronics in a cabinet above Achromat 08 with the Dimtel front/back-end unit, the Dimtel iGp12 signal processing units, the longitudinal stripline back-end, and the R&S BBA150 amplifiers.

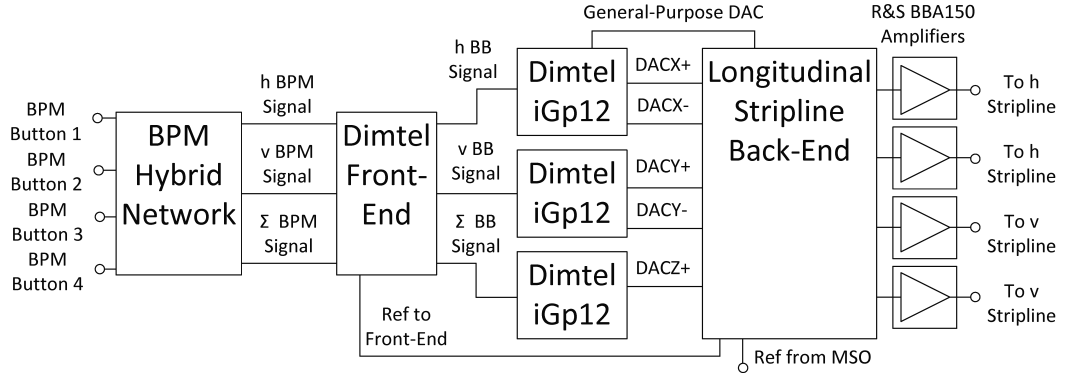


Figure 39: A somewhat simplified block diagram of the BBB feedback system in the 3 GeV ring. Note that this set-up is used when applying longitudinal feedback with the striplines, and not with the overloaded cavity.

5.1.4 Complete Set-up

Figure 39 shows a block diagram of the BBB feedback set-up in the 3 GeV ring. Figure 30, 31, 32, and 34 show the block/circuit diagrams of the sub components. The feedback signals to the striplines are amplified by four Rohde & Schwarz BBA150 wideband amplifiers [22]. These amplifiers can deliver an rms RF power of at least 200 W in a frequency span from 9 kHz to 250 MHz. Thus they can be used for both providing transverse feedback in the BB range and for longitudinal feedback in the 150 - 250 MHz range (see Figure 33). This is the set-up that has been used this far. After the 2017 summer shut-down, the longitudinal feedback will be provided by the cavity, and the longitudinal stripline back-end will no longer be needed. The transverse feedback signals, DAC(X/Y)(+/-), are then fed directly to the striplines via the amplifiers. The longitudinal common-mode feedback signal, DACZ+, will be upconverted to the 600-650 MHz range in the Dimtel front/back-end unit and fed to the cavity as shown in Figure 17. Commercial UHF amplifiers will be used to drive the cavity.

The two striplines and the button BPM are installed in Achromat 08 (the 3 GeV ring has 20 achromats in total). They are shown in the ring tunnel in Figure 40. The overloaded cavity has recently been installed in Achromat 11, as seen in Figure 41. Figure 38 shows the BBB electronics installed in a cabinet just above Achromat 08.

5.2 BBB Feedback in the 1.5 GeV Ring

The 1.5 GeV ring is equipped with the same Dimtel signal processing units as in the 3 GeV ring. The Dimtel front/back-end unit is here operating at 1.5 GHz compared to 1 GHz in the 3 GeV ring. While the front-end has been connected to a BPM, no actuators have yet been connected to the system. Thus, it is possible to monitor the beam motion with the system, but not applying any feedback. However, it has been

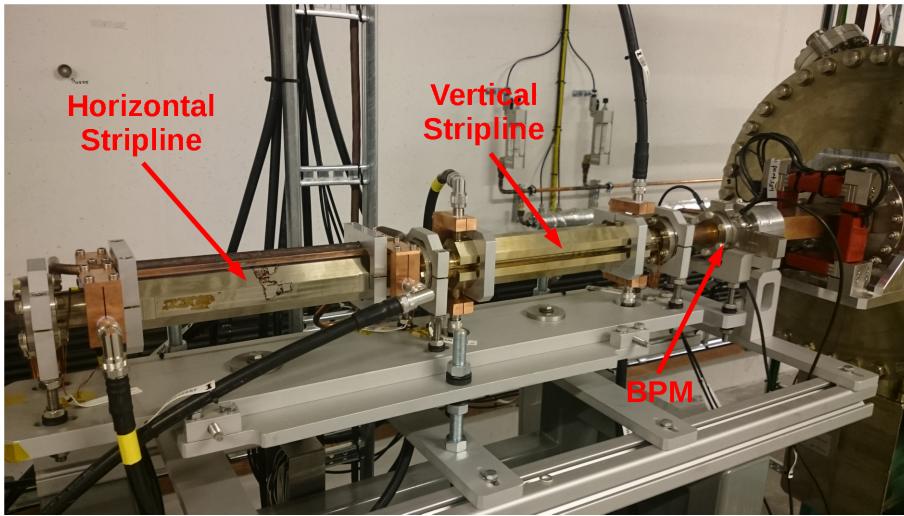


Figure 40: The two striplines and the button BPM installed in Achromat 08.

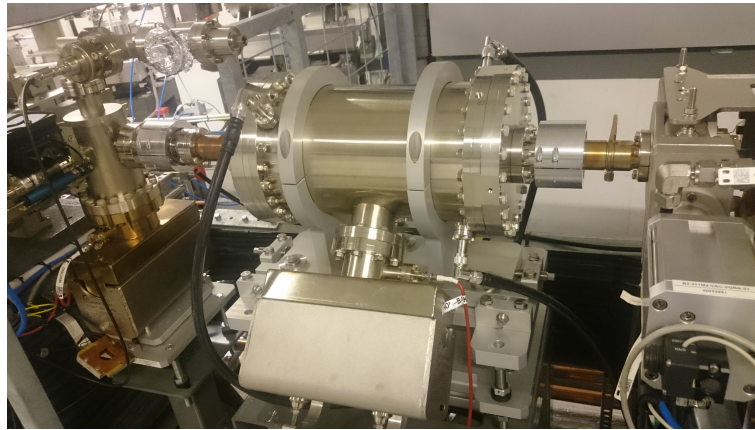


Figure 41: The cavity when it is installed in Achromat 11.

possible to keep the beam stable at beam currents above 150 mA in the longitudinal plane, even without feedback. This was achieved by injecting with an unstable beam up to approximately 150 mA with the Landau cavities tuned in. At this current, the induced fields in the Landau cavities are large enough to provide enough bunch lengthening and Landau damping to make the beam longitudinally stable. This is only possible at certain cavity temperatures where the dangerous HOMs are shifted away from the spectrum of the CBMs. It has not yet been possible to use the same technique in the 3 GeV ring to keep a longitudinal stable beam at high currents. One explanation can be that the harmonic number is 176 in the 3 GeV ring and 32 in the 1.5 GeV ring, giving a 5.5 denser CBM spectrum in the former (see Section 2.1). Another explanation is that the longitudinal CBMIs are driven by HOMs in the main and Landau cavities, and there are at date twice as many cavities in the 3 GeV ring.

It has thus far not been possible to keep the beam stable in the horizontal and vertical plane at higher currents in the 1.5 GeV ring, so feedback will eventually be needed. After the 2017 summer shut-down, feedback will be applied in all three planes via the diagnostic stripline [20]. Here, the longitudinal BB signal has to be upconverted, and a back-end for that purpose has to be constructed.

6 Beam Measurements

In this section, some measurements on the electron beam are presented where different applications of the BBB feedback system are being used.

6.1 Diagnostic Measurements

Since the signal processing units record the beam motion over several turns, the BBB feedback system can be used as a comprehensive diagnostic tool. This can even be done in parallel with feedback operation. An example, the transverse tunes are obtained as an FFT of the beam motion and monitored by the MAX IV control system during operation.

The BBB feedback system can also create transients in the oscillation amplitudes of the bunches, which makes it possible to measure growth and damp times. The transients are generated by switching the filter settings in the feedback system. An example of a grow/damp transient measurement in the horizontal plane is shown in Figure 42. Here, the beam is horizontally unstable without feedback but stable when the feedback is running, thus $D - G < 0$ and $D + D_{\text{fb}} - G > 0$ in (2.7). The grow transient is generated when the feedback is turned OFF at $t = 0$. As seen in Figure 42 (a), the oscillation amplitudes of all the 176 bunches grow exponentially until $t = 25$ ms when the feedback is turned ON again. After that, the oscillation amplitudes of the bunches are damped exponentially. Since the oscillations of each single bunch are recorded during the grow/damp transient, it is possible to do a mode analysis to find which of the CBMs that are driving the instability. This is shown in Figure 42 (b), where the mode spectrum is plotted. As seen, CBM #152 is driving the instability, and this mode is excited by a cavity HOM. During this measurement, the growth rate measured when $0 < t < 25$ ms was $D - G = -0.29$ 1/ms, while the damping rate when $t > 25$ ms was $D + D_{\text{fb}} - G = 2.50$ 1/ms.

Grow/damp measurements have been particularly useful when suppressing longitudinal CBMs by shifting the frequencies of the cavity HOMs, as described in Section 2.3.4. If instead the beam is naturally stable ($D - G > 0$), one can drive the bunches with positive feedback ($D_{\text{fb}} < 0$) until they oscillate with a relatively large amplitude, and then turn OFF the feedback and measure the damping time as the oscillations decay. This is known as a drive/damp measurement.

More diagnostic applications for a BBB feedback system are described in [17].

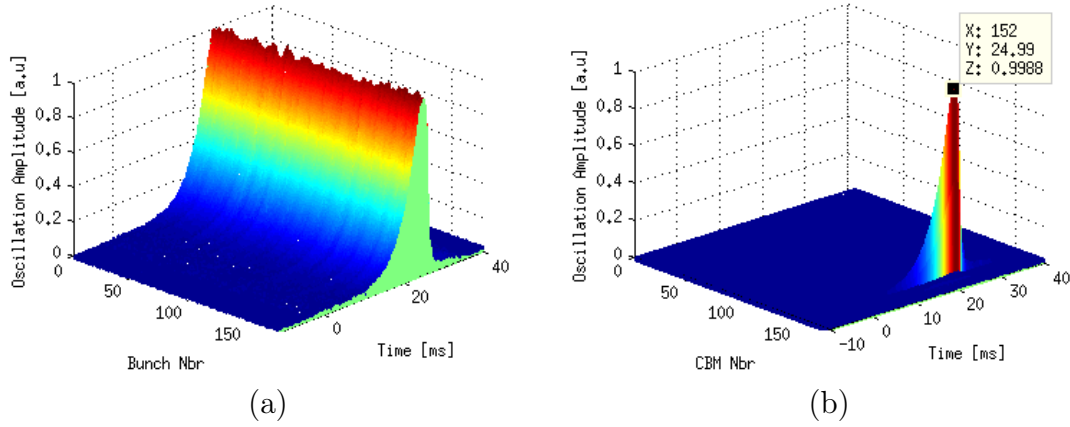


Figure 42: (a) shows the evolution of the oscillation amplitude for each bunch during a horizontal grow/damp measurement. The horizontal feedback is turned OFF at $t = 0$ ms, and turned ON again at $t = 25$ ms. (b) shows the evolution of the CBMs during the measurement. As seen, the instability is caused by CBM #152.

6.2 Bunch Cleaning

As mentioned in Section 2.3.5, there are several advantages of operating with non-uniform filling pattern. The BBB feedback system can perform bunch cleaning where individual bunches are driven at their betatron frequency until they oscillate with so large amplitudes that they hit the physical boundaries of the beam chambers and are lost. At MAX IV, the bunch cleaning is often performed in the vertical plane, and the unwanted bunches are dumped at a vertical scraper that is inserted close to the beam. As an example, Figure 43 shows the measured filling pattern for the uniform filled ring, and when 8 populations, each with 11 bunches, are kept. In [10], it is reported that bunch cleaning has been used to perform single-bunch experiments.

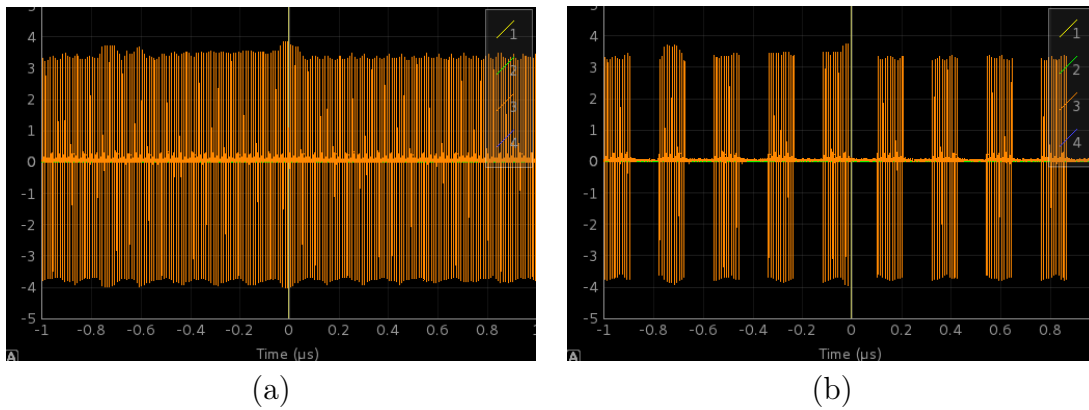


Figure 43: The filling pattern measured from the bi-polar BPM signal with an oscilloscope. (a) shows an almost uniform filling pattern, while (b) shows the filling pattern when 8 populations, each with 11 bunches, are kept.

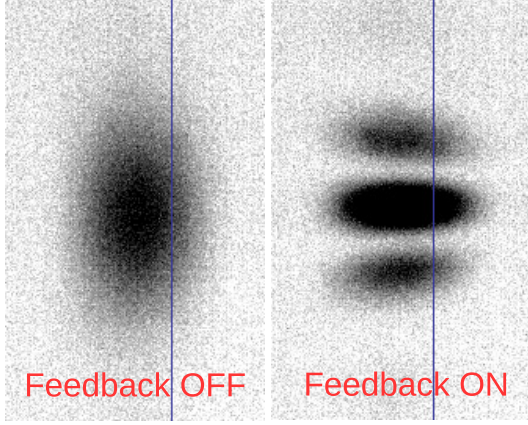


Figure 44: The diffracted transverse beam profile measured at the diagnostic beamline when the vertical feedback is turned ON and OFF. The CBMIs are here driven by ions.

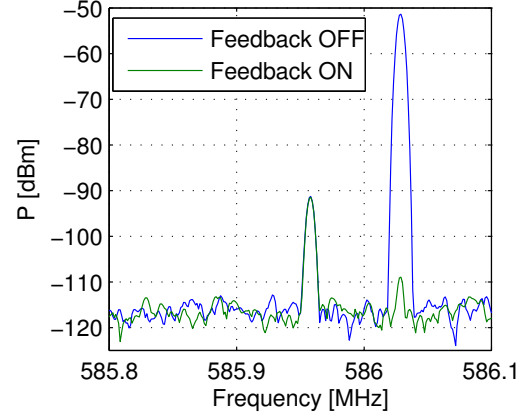


Figure 45: The horizontal beam spectrum around the 1032:nd revolution harmonic, with the horizontal feedback ON and OFF. CBM #152 is excited which is driven by a cavity HOM.

6.3 Feedback Effect on Beam Quality

As mentioned, the BBB feedback system is a comprehensive diagnostic tool that can be used for many types of beam studies. However, in the end, its most important task is to suppress CBMIs and thereby make sure that the effective emittance and energy spread of the beam are kept at their design values. Some examples where the beam properties are measured, with and without, feedback are now presented.

6.3.1 Transverse Feedback

During the early commissioning of the 3 GeV ring, ion-induced instabilities in both the horizontal and in the vertical plane were detected at beam currents as low as 30-40 mA. These CBMIs have this far been relatively weak, and it has been possible to suppress them with feedback. Figure 44 shows the transverse beam profile measured at the diagnostic beamline in Achromat 20, with and without feedback, when a vertical ion-driven CBMI is excited. The beam profile is here obtained from the synchrotron light radiating from a dipole magnet that is projected on a CCD camera [8]. As seen, the vertical beam size, and thereby the effective vertical emittance, is blown up when the feedback is turned OFF. The threshold where the ion-driven CBMIs appear has steadily moved towards higher beam currents as the quality of the vacuum has improved. They were rarely seen at currents below 100 mA in June 2017.

CBMIs that are driven by trapped transverse high-Q eigenmodes in the cavities, have also been observed. As an example, Figure 45 shows the horizontal beam spectrum around the 1032:nd ($5 \cdot 176 + 152$) revolution harmonic when the feedback is turned ON and OFF. The spectrum is obtained with a spectrum analyser and the BPM receiving network described [20]. The CBM is found at 586.0289 MHz, and

its spectrum line is suppressed by more than 50 dB when the feedback is running. Note that the magnitude of the revolution harmonic at 585.9582 MHz is unchanged by the feedback (as it should). The RF frequency and horizontal fractional tune during the measurement were $f_{\text{RF}} = 99.9308$ MHz and $\nu = 0.1246$, respectively, and we see from (2.6) that it is CBM #152 ($m = 152$) that is excited. Note that this is the same mode that was excited during the grow/damp measurement in Figure 42.

6.3.2 Longitudinal Feedback

The longitudinal CBMIs have this far been driven by HOMs in the cavities, and it has been necessary to operate with feedback in this plane in order to keep the beam stable at higher currents. It is possible to measure the longitudinal bunch profile at the diagnostic beamline by measuring the temporal distribution of the dipole light with an optical sampling oscilloscope. As an example, Figure 46 shows the measured bunch profile at 70 mA, with and without longitudinal feedback ³. The Landau cavities are here completely detuned, and do not contribute to any bunch lengthening. The bunch profile should therefore be rather Gaussian which can be seen when the feedback is ON. When the feedback is turned OFF, the Gaussian-shaped bunches are oscillating in the longitudinal plane around their energy equilibrium which also results in an increased energy spread of the beam. Thus, the wider bunch profile measured with feedback OFF is not a result of any notable bunch lengthening, but mainly due to an oscillating beam and to the fact that the oscilloscope is unable to capture data from a single bunch at a single turn. The centroid of the unstable bunch is oscillating with a magnitude of approximately $\Delta T = \pm 200$ ps. This corresponds to $\Delta\phi = \pm 7.2$ degrees relative to the 100 MHz RF system. The synchrotron frequency, f_s during the measurement was 1.00 kHz, and with this parameter known, we can estimate that the dipole oscillation of the centroid corresponds to a relative energy oscillation, $\Delta W/W_0$, of

$$\frac{\Delta W}{W_0} = \frac{2\pi f_s}{\alpha} \Delta T = \pm 0.0041 \quad (6.1)$$

where $\alpha = 3.06 \cdot 10^{-4}$ is the momentum compaction factor of the ring. The natural energy spread of the bare lattice is $7.7 \cdot 10^{-4}$, so the dipole oscillations introduced by the longitudinal CBMI result in an additional energy spread of the beam that is several times greater than that of a stable beam.

While measurements of the beam profile and beam spectrum show that CBMIs have a degrading effect on the beam quality, the ultimate measurement would be on the spectral lines at the beamlines since they comprise the light delivered to the users. Spectral measurements with longitudinal stable and unstable beams have been performed at the BioMAX beamline⁴. BioMAX is an X-ray macromolecular crystallography beamline where the photon energy range is 5-25 keV [5]. The X-ray source is an in-vacuum undulator with a magnetic length of 2 m, and with a minimum magnet gap of 4.2 mm.

³The measurement was assisted by Jens Sundberg

⁴The measurements at BioMAX were assisted by Roberto Appio and Thomas Ursby

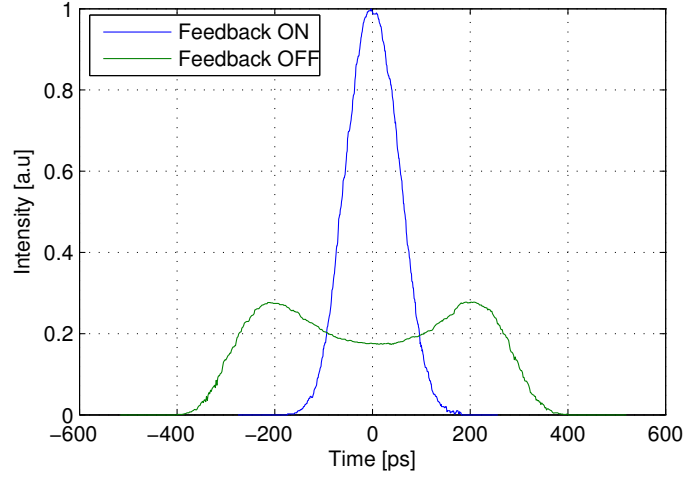


Figure 46: The bunch profile measured at the diagnostic beamline at a 70 mA, with longitudinal feedback ON and OFF. Note that the wider profile measured with feedback OFF is mainly a result of the bunches oscillating around their energy equilibrium, and not due to bunch lengthening.

One measurement series was performed in April 2017 around the 7:th harmonic spectral line. The beamline configuration was the same that has been used during beam delivery to some of the first users. Figure 47 shows the measured photon flux at a beam current of 37 mA with longitudinal feedback ON and OFF. As seen, the spectral line is wider and the peak flux is decreased when the beam is unstable in the longitudinal plane due to the increased effective energy spread. A simulation of the photon flux with the same beamline parameters was performed in SPECTRA [23]. The simulation results can also be seen in Figure 47 where the peak flux has been normalized to that of the stable beam. There is an excellent agreement to the measurement. The spectrum was also measured at a beam current of 3.3 mA (see Figure 47), and the current is here so low that the beam remains stable even without feedback. The normalized flux for the stable beam at 37 mA and 3.3 mA are plotted in Figure 48. As seen, the line widths look very similar for the two curves, and one can therefore conclude that the properties of a beam that is stabilized with feedback is very similar to that of a beam that is naturally stable.

The magnitude of the dipole oscillations for the unstable beam in Figure 47 is not as large as during the bunch profile measurements shown in Figure 46. A measurement series at BioMAX, with larger dipole oscillations, was performed in November 2016. The results can be seen in Figure 49. Here, the 5:th harmonic spectral line is measured at a beam current of 12 mA. The reason why the oscillations are larger during this measurement, despite that the beam current is a factor three lower, is mainly because more dangerous cavity HOMs are here overlapping the spectrum of the CBMs (see Section 2.3.4). The two peaks of the unstable beam are found at approximately ± 0.06 keV from the 5:th harmonic spectral line of 8.92 keV.

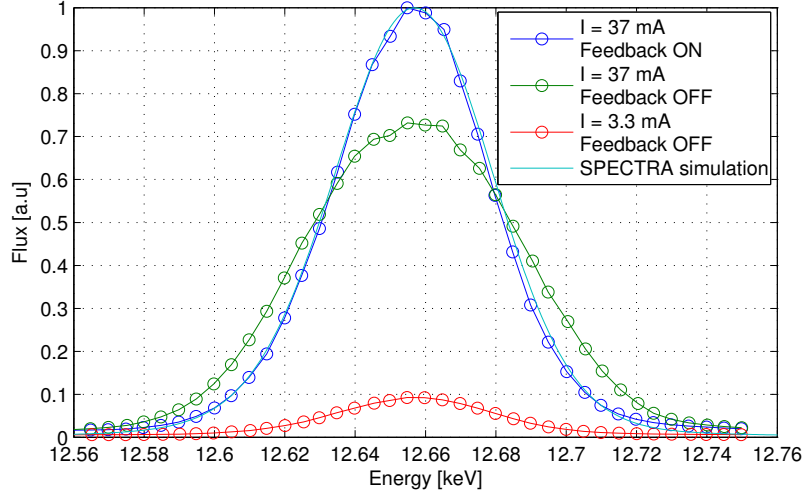


Figure 47: The photon flux around the 7:th harmonic spectral line at the BioMAX beamline measured in April 2017. The results are compared to a SPECTRA simulation.

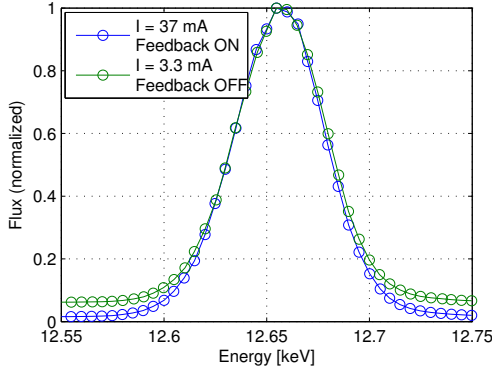


Figure 48: The normalized photon flux around the 7:th harmonic spectral line of a naturally stable beam at 3.3 mA and of a stabilized beam at 37 mA. It is the same measurement as in Figure 47.

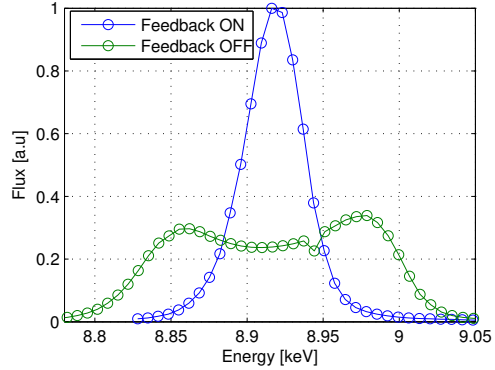


Figure 49: The measured photon flux around the 5:th harmonic spectral line. The measurement was performed at the BioMAX beamline in November 2016 at a beam current of 12 mA.

The photon wavelength of the k :th harmonic spectral line can be approximated as

$$\lambda_k = \frac{\lambda_u}{2k\gamma^2} \left(1 + \frac{K^2}{2} + \gamma^2\vartheta^2 \right) \quad (6.2)$$

where λ_u is the undulator magnetic period, γ the Lorentz factor, K is the undulator/wiggler parameter, and ϑ is the observation angle from the forward direction of the emitted synchrotron radiation [28]. The photon energy is then given by $E = \hbar c_0 / \lambda_k$, where c_0 is the speed of light and \hbar is the Planck constant. We can see that the sizes of the collimators used during the measurements are very small since

the spectral lines of the stable beams in Figure 47-49 look quite symmetrical. Thus, the spectrum is close to that of a pin-hole spectrum, and the red-shift due to the Doppler effect (ϑ is small in (6.2)) has little effect on the observed spectrum. The corresponding relative energy oscillation of the bunch centroid during the measurement is estimated to approximately $\Delta W/W_0 = \pm 0.0034$ when using (6.2). Here, $\lambda_w = 1.8$ cm, $k = 5$, and $K = 1.825$. It is also assumed that $\vartheta = 0$ (the horizontal and vertical design dispersion at the undulator is zero).

7 Conclusions and Future Work

It has been observed that the CBMIs have a degrading effect on the quality of the beam in the two MAX IV storage ring. A BBB feedback system has been installed in the 3 GeV ring for suppression of CBMIs, and it has this far been possible to keep a stable beam at currents above 100 mA. Two stripline kickers have been manufactured, and they have provided feedback in all three planes. A WG overloaded cavity kicker that is dedicated for longitudinal feedback has also been designed and manufactured, but has not yet been commissioned.

After the 2017 summer shut-down, the WG overloaded cavity will be commissioned, and this will hopefully make it easier to achieve a longitudinally stable beam at higher currents. The BBB feedback system in the 1.5 GeV ring will also be commissioned during the autumn of 2017. The ultimate goal is to deliver light to the users in both storage rings with stable beams at the design current of 500 mA.

Acknowledgements

The authors would like to thank Karl Åhnberg for doing the mechanical design of the striplines and the cavities. Thanks to Henrique de Oliveira Caiafa Duarte and Sergio Rodrigo Marques at LNLS, Nikolas Heurich at ELSA, and Alun Morgan at Diamond for sharing ideas on the mechanical design of the cavity. Thanks to Eshraq Al Dmour, Marek Grabski, Mathieu Leme, and Esa Paju in the vacuum group for the support and expertise in the design and assembly phase of the cavity. Thanks to Anders Bjermo, Lars Christiansson, and Dirk Winnat for the workshop support. Thanks to Jens Sundberg for his support at the diagnostic beamline. Thanks to Roberto Appio, Hamed Tarawneh, and Thomas Ursby for their help during the measurements at BioMAX. Also big thanks to Dmitry Teytelman at Dintel for all the support with the BBB feedback system.

Finally, a special thanks to Åke Andersson, Francis Cullinan, and Pedro Fernandes Tavares for all the help during the commissioning of the BBB feedback system and for all the hours spent in the control room, fighting those damn cavity HOMs!

References

- [1] N. P. Abreu, R. H. A. Farias, and P. F. Tavares. “Longitudinal dynamics with rf phase modulation in the brazilian electron storage ring”. *Physical Review Special Topics: Accelerators and Beams* 9 (2006).
- [2] Å. Andersson et al. “The 100 mhz rf system for the max iv storage rings”. In: *2nd International Particle Accelerator Conference*. 2011, pp. 193–195.
- [3] J. Andersson and D. Olsson et al. “New features of the max iv thermionic pre-injector”. *Nuclear Instruments and Methods in Physics Research* 855 (2017), pp. 65–80.
- [4] C. Belver-Aguilar et al. “Stripline design for the extraction kicker of compact linear collider damping rings”. *Physical Review Special Topics: Accelerators and Beams* 17 (2014).
- [5] *BioMAX website*. <https://www.maxiv.lu.se/accelerators-beamlines/beamlines/biomax/>.
- [6] J. Björklund-Svensson. “Master thesis: characterization of higher order modes in the max iv active 100 mhz cavities” (2015).
- [7] R. Boni et al. “A waveguide overloaded cavity as longitudinal kicker for the daphne bunch-by-bunch feedback system”. In: *Particle Accelerators*. 1996, pp. 95–113.
- [8] J. Breunlin and Å. Andersson. “Emittance diagnostics at the max iv 3 gev storage ring”. In: *7th International Particle Accelerator Conference*. 2016, pp. 2908–2910.
- [9] *COMSOL Multiphysics website*. <http://www.comsol.com/>.
- [10] F. J. Cullinan et al. “Impedance characterization and collective effects in the max iv 3 gev ring”. In: *North American Particle Accelerator Conference*. 2016.
- [11] *Dimtel website*. <http://www.dimtel.com/>.
- [12] *FMB Berlin website*. <http://www.fmb-berlin.de>.
- [13] *GdfidL website*. <http://www.gdfidl.de>.
- [14] D. A. Goldberg and G. R. Lambertson. “Dynamic devices a primer on pickups and kickers”. In: *AIP Conference Proceedings*. 1992, pp. 537–600.
- [15] N. Heurich et al. “A longitudinal kicker cavity for a bunch-by-bunch feedback system at elsa”. In: *2nd International Particle Accelerator Conference*. 2011, pp. 480–486.
- [16] Y. M. Kang and R. L. Kustom. “Hom damping with coaxial dampers in the storage ring cavities of the advanced photon source”. In: *4th European Particle Accelerator Conference*. 1994.
- [17] M. Lonza and H. Schmickler. “Multi-bunch feedback systems”. In: *CAS-CERN: Advanced Accelerator Physics, Trondheim, Norway*. 2014, pp. 503–546.

- [18] A. F. D. Morgan and G. Rehm. “Design for the diamond longitudinal bunch-by-bunch feedback cavity”. In: *5th International Beam Instrumentation Conference*. 2016, pp. 340–343.
- [19] K. Y. Ng. *Physics of Intensity Dependent Beam Instabilities*. World Scientific Publisher, 2005.
- [20] D. Olsson, A. Karlsson, and L. Malmgren. *Design of Striplines for the MAX IV and SOLARIS Storage Rings*. Tech. rep. LUTEDX/(TEAT-7254)/(2017). Lund Institute of Technology, 2017.
- [21] R. Lindvall, *priv. comm.* (June 2017).
- [22] Rohde & Schwarz website. <http://www.rohde-schwarz.com>.
- [23] SPECTRA website. <http://www.radiant.harima.riken.go.jp/spectra/>.
- [24] T. Günzel, *priv. comm.* (Oct 2016).
- [25] M. Takao et al. “Observation of ion effects at the spring-8 storage ring”. In: *8th European Particle Accelerator Conference*. 2002, pp. 1562–1564.
- [26] P. F. Tavares et al. “The max iv storage ring project”. *Journal of Synchrotron Radiation* 21 (2014), pp. 862–877.
- [27] H. Wang and J. Guo. “Bead-pulling measurement principle and technique used for the srf cavities at jlab”. In: *USPAS Education in Beam Physics and Accelerator Technology, SRF Practices and Hands-on Measurements, Thomas Jefferson Lab, USA*. 2015.
- [28] H. Wiedemann. *Particle Accelerator Physics*. Third. Springer-Verlag, 2007.
- [29] W. Z. Wu et al. “Development and commissioning of bunch-by-bunch longitudinal feedback system for duke storage ring”. In: *23rd Particle Accelerator Conference*. 2009, pp. 4117–4119.
- [30] W. Wu. “Ph.d. thesis: feedback systems for control of coupled-bunch instabilities in the duke storage ring” (2012).

Appendix A Stripline S-parameter Measurements

Figure 50-57 show the measured mixed-mode S-parameters of the two striplines. The measurement set-up with the physical and logical ports are the same as described in [20]. Here, all the 2x16 parameters are not shown since $S_{dc11} \approx S_{cd11}$, $S_{dc22} \approx S_{cd22}$, $S_{dd21} \approx S_{dd12}$, $S_{cc21} \approx S_{cc12}$, $S_{dc21} \approx S_{cd12}$, and $S_{dc12} \approx S_{cd21}$.

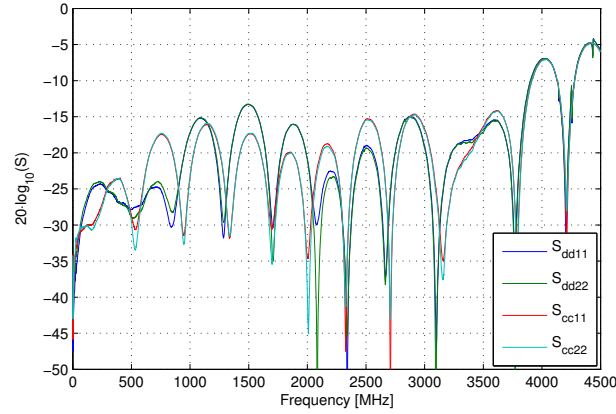


Figure 50: Differential and common-mode reflection coefficients of the horizontal stripline.

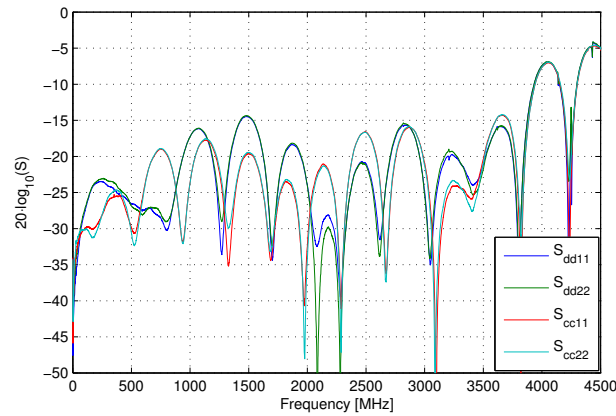


Figure 51: Differential and common-mode reflection coefficients of the vertical stripline.

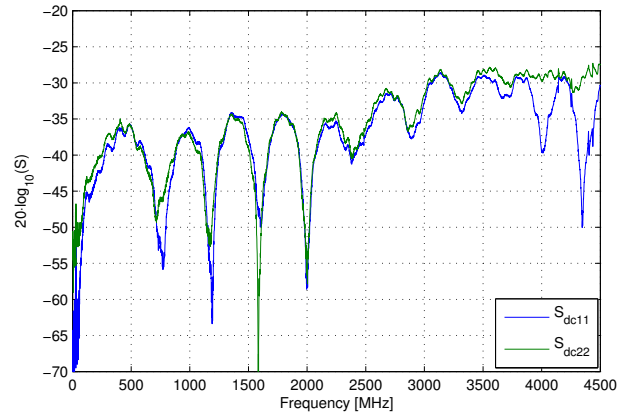


Figure 52: Cross-mode reflection coefficients of the horizontal stripline.

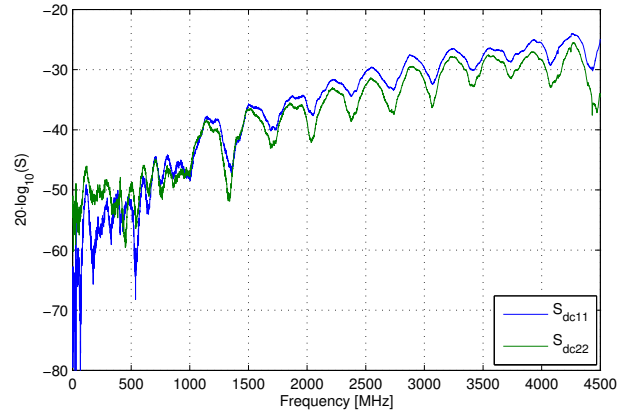


Figure 53: Cross-mode reflection coefficients of the vertical stripline.

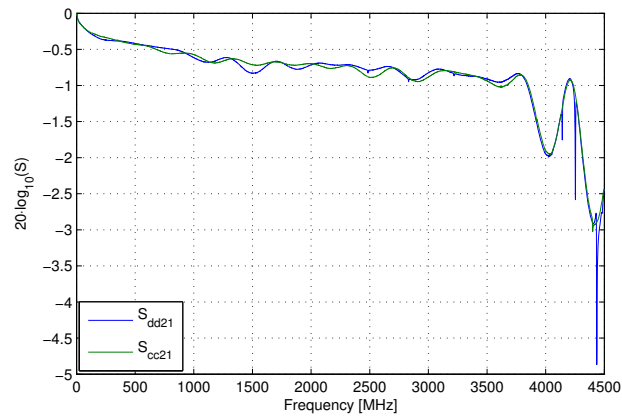


Figure 54: Differential and common-mode transmission coefficients of the horizontal stripline.

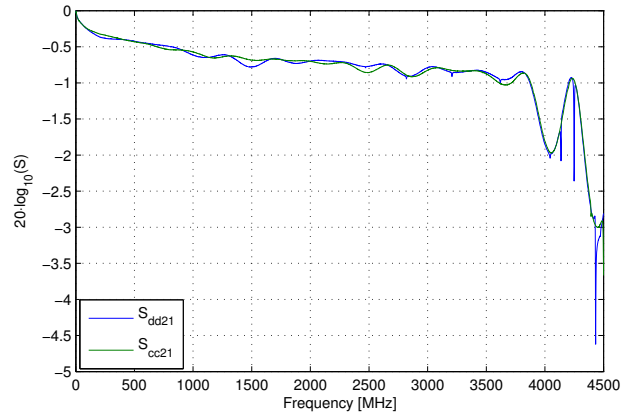


Figure 55: Differential and common-mode transmission coefficients of the vertical stripline.

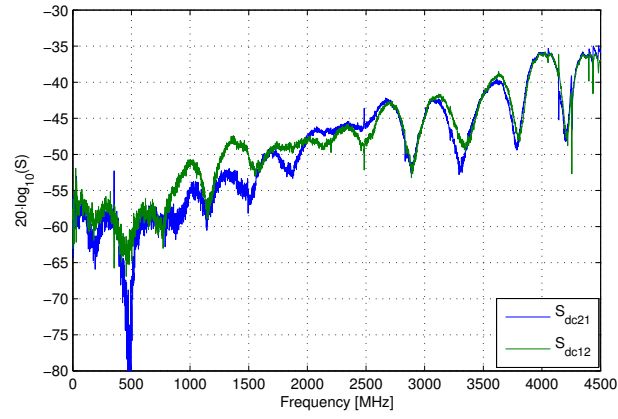


Figure 56: Cross-mode transmission coefficients of the horizontal stripline.

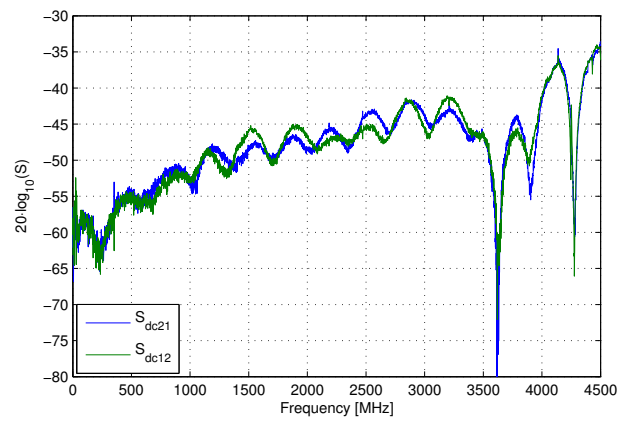


Figure 57: Cross-mode transmission coefficients of the vertical stripline.